HeLa cells with the genes for chimeric fluorescent proteins designed to stain different subcellular structures: mitochondria (mSECFP-mit), actin (Venus-Actin), and the nucleus (mRFP1-nu). The HeLa cells were then observed using the CSU10 system with a mercury arc lamp and a half-reflective mirror (Fig. 6C). The three emission signals from the different fluorescent proteins were precisely separated from each other and merged. As shown in Fig. 6C, the three images were well aligned spatially.

We next demonstrated time-lapse imaging of three different colors using the same microscopy system. To monitor the translocation of protein kinase C gamma (PKC-γ) and its upstream Ca^{2+} signal in a living cell, DsRed T3 fused with PKC-γ (PKC-γ-DsRed T3) and yellow cameleon 3.60 (YC3.60) were co-expressed in HeLa cells. YC3.60 is a genetically encoded Ca^{2+} indicator that changes the ratio of YFP and CFP intensity by nearly 600%, based on FRET technology (Nagai *et al.*, 2004). PKC-γ is an isozyme of conventional PKC (cPKC) and has functional C1 and C2 domains in its regulatory region, which bind diacylglycerol and Ca^{2+}, respectively (Nishikawa *et al.*, 1997). Ca^{2+}-mediated PKC-γ activation and translocation to the plasma membrane are well studied (Sakai *et al.*, 1997). Fig. 6D shows a series of pseudo-colored images of HeLa cells expressing YC3.60 (upper panel) and PKC-γ-DsRed T3 (lower panel). The PKC-γ translocation to the plasma membrane was precisely synchronized with the increase in cytoplasmic Ca^{2+} concentration after the application of 10 μM histamine. This result agrees with the previously reported Ca^{2+}-controlled transient membrane association of PKC (Violin *et al.*, 2003).

In this paper, we demonstrated the usefulness of multiple-point scanning confocal microscopy using a 100 W mercury arc lamp as a light source. In our new system, the coupling efficiency between the multi-mode optical fiber and the CSU10 was about 0.01, which is lower than that of CARV II (0.05–0.07), another Nipkow disk-scanning confocal system (Toomre and Pawley, 2006). In spite of the low coupling efficiency, the power of the excitation light with no prominent emission lines of the mercury arc lamp was adequate for high-speed Ca^{2+} imaging at 100 Hz (Fig. 5). In addition, using CSU10 with a mercury arc lamp and a half-reflective mirror may solve the problems associated with multi-color imaging using a laser light source, such as the limitation of fluorophore choice. Many variants of fluorescent proteins have been developed and are available (Giepmans *et al.*, 2006). In particular, red to far-red emitting bright fluorescent proteins have emerged (Merzlyak *et al.*, 2007; Shcherbo *et al.*, 2007). In multi-color imaging, these newly developed red fluorescent proteins are anticipated to be good FRET partners for conventional fluorescent proteins, such as ECFP, EGFP, and EYFP. When we use fluorescent protein variants with longer emission wavelengths, we find that a Xenon arc lamp is superior to the mercury arc lamp, owing to the incident wavelengths expanding to the far-red region. In such cases, a Xenon arc lamp can easily replace the mercury arc lamp as the light source in our microscopy system. Thus, this microscopy system should make multi-color imaging readily available to many researchers.

Acknowledgements. We are grateful to R.Y Tsien for the gift of the mRFP1 plasmid, and we would like to thank M. Shimizu and H. Hirukawa (Yokogawa Electric Corporation) and M. Mizuta and K. Toshimitsu (Nikon Corporation) for technical support and advice. This work was partly supported by Grants from Scientific Research on Advanced Medical Technology of the Ministry of Labor, Health and Welfare of Japan, and the Japanese Ministry of Education, Science and Technology.

References

Bevis, B.J. and Benjamin, S.G. 2002. Rapidly maturing variants of the Discosoma red fluorescent protein (DsRed). *Nat. Biotechnol.*, **20**: 83–87.

Campbell, R.E., Tour, O., Palmer, A.E., Steinbach, P.A., Baird, G.S., Zacharias, D.A., and Tsien, R.Y. 2002. A monomeric red fluorescent protein. *Proc. Natl. Acad. Sci. USA*, **99**: 7877–7882.

Fewer, D.T., Hewlett, S.J., and McCabe, E.M. 1998. Laser sources in direct-view-scanning, tandem-scanning, or Nipkow-disk-scanning confocal microscopy. *Applied Optics*, **37**: 380–385.

Genka, A., Ishida, H., Ichimori, K., Hirota, Y., Tanaami, T., and Nakazawa, H. 1999. Visualization of biphasic Ca^{2+} diffusion from cytosol to nucleus in contracting adult rat cardiac myocytes with an ultra-fast confocal imaging system. *Cell Calcium*, **25**: 199–208.

Giepmans, B.N.G., Adams, S.R., Ellisman, M.H., and Tsien R.Y. 2006. The fluorescent toolbox for assessing protein location and function. *Science*, **312**: 217–224.

Hibbs, A. 2004. Chapter 3-Hardware. In *Confocal Microscopy for Biologists* (A. Hibbs, ed.), Kluwer Academic/Plenum Publishers, New York, pp.90–99.

Ichihara, A., Tanaami, T., Isozaki, K., Sugiyama, Y., Kosugi, Y., Mikuriya, K., Abe, M., and Uemura, I. 1996. High-speed confocal fluorescence microscopy using a Nipkow scanner with microlenses — for 3-D imaging of single fluorescence molecule in real time. *Bioimages*, **4**: 57–62.

Inoué, S. and Inoué, T. 2002. Direct-view high-speed confocal scanner: the CSU-10. *Methods Cell Biol.*, **70**: 87–127.

Kam, Z., Jones, M., Chen, H., Agard, D., and Sedat, J. 1993. Design and construction of an optimal illumination system for quantitative wide-field multi-dimensional microscopy. *Bioimaging*, **1**: 71–81.

Matsuda, T., Miyawaki, A., and Nagai, T. 2008. Direct measurement of protein dynamics inside cells using a rationally designed photoconvertible protein. *Nat. Methods*, **5**: 339–345.

Merzlyak, E., Goedhart, J., Shcherbo, D., Bulina, M., Shcheglov, A., Fradkov, A., Gaintzeva, A., Lukyanov, K., Lukyanov, S., Gadella T., and Chudakov, D. 2007. Bright monomeric red fluorescent protein with an extended fluorescence lifetime. *Nat. Methods*, **4**: 555–557.

Nagai, T., Ibata, K., Park, E.S., Kubota, M., Mikoshiba, K., and Miyawaki, A. 2002. A variant of yellow fluorescent protein with fast and efficient maturation for cell-biological applications. *Nat. Biotechnol.*, **20**: 87–90.

Nagai, T., Yamada, S., Tominaga, T., Ichikawa, M., and Miyawaki, A. 2004. Expanded dynamic range of fluorescent indicators for Ca^{2+} by circularly permuted yellow fluorescent proteins. *Proc. Natl. Acad. Sci. USA*, **101**: 10554–10559.

Nishikawa, K., Toker, A., Johannes, F.J., Zhou, S.Y., and Cantley, L.C. 1997. Determination of the specific substrate sequence motifs of protein kinase C isozymes. *J. Biol. Chem.*, **272**: 952–960.

Sakai, N., Sasaki, K., Ikegaki, N., Shirai, Y., Ono Y., and Saito, N. 1997. Direct visualization of the translocation of the gamma-subspecies of

protein kinase C in living cells using fusion proteins with green fluorescent protein. *J. Cell Biol.*, **139**: 1465–1476.

Shcherbo, D., Merzlyak, E., Chepurnykh, T., Fradkov, A., Ermakova, G., Solovieva, E., Lukyanov, K., Bogdanova, E., Zaraisky, A., Lukyanov, S., and Chudakov, D. 2007. Bright far-red fluorescent protein for whole-body imaging. *Nat. Methods*, **4**: 741–746.

Swedlow, J.R., Andrews, P.D., and Platani, M. 2004. Chapter 17-*In vivo* imaging of Mammalian Cells. In Live Cell Imaging, A Laboratory Manual (R. Goldman and D. Spector, eds.). Cold Spring Harbor Laboratory Press, New York, pp.329–343.

Tani, T., Miyamoto, Y., Fujimori, K.E., Taguchi, T., Yanagida, T., Sako, Y., and Harada, Y. 2005. Trafficking of a ligand-receptor complex on the growth cones as an essential step for the uptake of nerve growth factor at the distal end of the axon: A single-molecule analysis. *J. Neurosci.*, **25**: 2181–2191.

Toomre, D. and Pawley, J. 2006. Disk-Scanning Confocal Microscopy. In *Handbook of biological Confocal Microscopy* (J. Pawley, ed.), SpringerScience+Business Media, New York, pp.221–238.

Violin, J.D., Zhang, J., Tsien, R.Y., and Newton, A.C. 2003. A genetically encoded fluorescent reporter reveals oscillatory phosphorylation by protein kinase C. *J. Cell Biol.*, **161**: 899–909.

Wang, E., Babbey, C., and Dunn, K. 2005. Performance comparison between the high-speed Yokogawa spinning disc confocal system and single-point scanning confocal systems. *J. Microsc.*, **218**: 148–159.

(Received for publication March 31, 2008 and accepted July 30, 2008)

Journal of Biotechnology 137 (2008) 1–7

Contents lists available at ScienceDirect

Journal of Biotechnology

journal homepage: www.elsevier.com/locate/jbiotec

A high-throughput and single-tube recombination of crude PCR products using a DNA polymerase inhibitor and type IIS restriction enzyme

Ippei Kotera[a], Takeharu Nagai[b,*]

[a] PRESTO, Japan Science and Technology Agency, 4-1-8 Honcho Kawaguchi, Saitama 332-0012, Japan
[b] Laboratory for Nanosystems Physiology, Research Institute for Electronic Science, Hokkaido University, Kita-20 Nishi-10 Kita-ku, Sapporo, Hokkaido 001-0020, Japan

Journal of Biotechnology 137 (2008) 1–7

Contents lists available at ScienceDirect

Journal of Biotechnology

journal homepage: www.elsevier.com/locate/jbiotec

A high-throughput and single-tube recombination of crude PCR products using a DNA polymerase inhibitor and type IIS restriction enzyme

Ippei Kotera [a], Takeharu Nagai [b,*]

[a] PRESTO, Japan Science and Technology Agency, 4-1-8 Honcho Kawaguchi, Saitama 332-0012, Japan
[b] Laboratory for Nanosystems Physiology, Research Institute for Electronic Science, Hokkaido University, Kita-20 Nishi-10 Kita-ku, Sapporo, Hokkaido 001-0020, Japan

ARTICLE INFO

Article history:
Received 31 March 2008
Received in revised form 22 June 2008
Accepted 7 July 2008

Keywords:
DNA manipulations
DNA recombination
DNA cloning
Type IIS restriction endonuclease
High-throughput

ABSTRACT

Type IIS restriction enzymes have been successfully used as "universal" restriction enzymes in DNA manipulations. We took a step further to develop a rapid technique for recombining DNA fragments, fully automatic single-tube recombination (FASTR), which enables multiple-fragment DNA recombination in a single step. Crude PCR products are directly mixed with both type IIS restriction endonuclease and DNA ligase to initiate a spontaneous and one-way recombination reaction. Highly efficient DNA recombination can be achieved by an inhibition of DNA polymerase with aphidicolin and a selective digestion of template DNAs by DpnI, a restriction enzyme to digest hemi-methylated DNA in the reaction solution; thereby the entire procedure takes less than 15 min. Owing to its simplicity, efficiency and rapidity, one-step FASTR can be applied to a wide range of DNA manipulations including those involving high-throughput applications where significant reduction in time and cost is expected.

1. Introduction

There have been various approaches to making cloning simpler or faster: instead of using classical restriction enzymes and DNA ligase, DNA recombination systems from different organisms have been used to manipulate plasmid DNA (Hartley et al., 2000; Liu et al., 1998). These techniques have made some repetitious gene clonings easier, but because they are based on DNA recombination, special sequences must accompany the gene to be cloned and the destination vector. These sequences are not removed during the recombination reaction, which is problematic when one tries to fuse one gene to another with a defined linker sequence. Another problem is that if a destination vector is not available for a certain application, one has to make it through conventional plasmid construction. Thus, recombination-based cloning techniques can lack to some degree the flexibility of classical cloning technology.

Type IIS restriction enzymes digest DNA sequence outside of their recognition sequence (Kleid et al., 1976; Takemori et al., 2002). With recognition sequences on primers, type IIS enzymes can be utilized as a universal restriction enzyme for the cloning of PCR products (Podhajska and Szybalski, 1985). We refocused on this classic enzyme because of its versatility and potential for a fast spontaneous DNA recombination reaction. With an inhibition of residual thermostable DNA polymerase activity and selective digestion of template DNAs, we are now able to recombine multiple DNA fragments directly from crude PCR solution in a single tube within 15 min.

2. Materials and methods

2.1. FASTR reaction

PCR was carried out using a high-fidelity thermostable DNA polymerase, KOD-plus (Toyobo, Osaka, Japan) according to the manufacturer's protocol. Briefly, the reaction buffer contained 1× KOD-plus buffer, 2 mM dNTPs, 25 mM $MgSO_4$, 1 unit of KOD-plus, 25 pmol each of forward/reverse primers, and 50 ng each of template plasmids, in a total volume of 50 μl. The template plasmids for mSECFP (Matsuda et al., 2008) and mVenus (Venus (Nagai et al., 2002) with A206K mutations (Zacharias et al., 2002)) were in a pcDNA3.0 vector (Invitrogen, CA, USA), and mCherry (Shu et al., 2006) was in a plant expression vector. pRSET B vector (Invitrogen, CA, USA) was modified by site-directed mutagenesis to delete an LguI site at nucleotide position 2830. The PCR conditions were as follows: 94 °C/2 min (94 °C/15 s, 60 °C/30 s, 68 °C/90 s), 35 cycles, 68 °C/5 min. One microliter of the PCR solution from each sample was transferred to a mixture containing the following reagents in a total volume of 20 μl: 17 mM Tris–acetate, 25 mM Tris–HCl (pH 7.5), 5 mM $MgCl_2$, 5 mM magnesium acetate, 33 mM potassium acetate, 5 mM ATP, 5 mM DTT, 63 μg/ml BSA, 5 U of LguI

* Corresponding author. Tel.: +81 11 706 3833; fax: +81 11 706 4968.
E-mail address: tnagai@es.hokudai.ac.jp (T. Nagai).

0168-1656/$ – see front matter © 2008 Elsevier B.V. All rights reserved.
doi:10.1016/j.jbiotec.2008.07.1816

(Fermentas, ON, Canada), 400 U of T4 DNA ligase (NEB, MA, USA), 20 U of DpnI (NEB, MA, USA), and 5 mM aphidicolin (Calbiochem, CA, USA). The mixture was incubated without agitation at room temperature for various lengths of time. After incubation, 5 μl of the mixture was used to transform *Escherichia coli* (JM109 DE3, Promega, WI, USA). The sequences of the primers used in the FASTR reaction were as follows: pRSET forward primer: GCTACTGCTCTTCGTGCGCTGGTACCATGGAATTCGAA, pRSET reverse primer: CTGATAGCTCTTCTCACGTACAGATCCCGACCCATTTG, GFP-variants forward primer: GCTAGCTCTTCAGTGATGGTGAGCAAGGGCGA and GFP-variants reverse primer: CTAGGCTCTTCTGCACTTGTACAGCTCGTCCATGC. For multiple-fragment FASTR the following sets of primers were used to amplify the inserts: GFP-variants forward 1: GCTAGCTCTTCAGTGATGGTGAGCAAGGGCGA, GFP-variants reverse 1: CTAGGCTCTTCTACCCTTGTACAGCTCGTCCATGC, GFP-variants forward 2: GCTAGCTCTTCAGGTATGGTGAGCAAGGGCGA, GFP-variants reverse 2: CTAGGCTCTTCTGCACTTGTACAGCTCGTCCATGC.

2.2. Fluorescent colony imaging

For the single-color imaging of mSECFP-expressed *E. coli* colonies, an LAS-1000plus image analyzer (Fujifilm, Tokyo, Japan) was used to take fluorescent images. For multicolor imaging, a hand-made device equipped with a Mercury lamp, interference filters, optical fiber cables, and video CCD camera (WAT-120N, Watec, Yamagata, Japan) was used. The filter combination was as follows: 440/21 excitation and 480/30 emission for mSECFP, 500/24 excitation and 535/26 emission for mVenus and 540/30 excitation and 575LP for mCherry. All images were acquired using ImageJ software. MetaMorph (Molecular Devices, CA, USA) was used for image analysis.

2.3. Determination of FRET efficiency

Venus/T-sapphire fusion protein was mixed with 0.05% trypsin–EDTA (Gibco, CA, USA) in PBS and incubated at 37 °C for 1 h. The samples with and without trypsin were analyzed by F-2500 fluorescence spectrophotometer (Hitachi, Tokyo, Japan). The peak values of the donor protein (T-sapphire) before and after the trypsin treatment were used to calculate the FRET efficiency, according to the following equation:

$$E = 1 - \frac{F_{DA}}{F_A}$$

where E is the FRET efficiency of the donor/acceptor pair, F_{DA} is the fluorescence intensity of the donor in the presence of the acceptor (before trypsin treatment), and F_A is the fluorescence intensity of the donor in the absence of the acceptor (after trypsin treatment).

3. Results

3.1. The concept of the FASTR reaction

The DNA cleavage site of type IIS endonucleases is at a distance from their DNA recognition site, thus these enzymes create DNA overhangs of any nucleotide sequence (Szybalski et al., 1991). This feature is advantageous for DNA manipulation in many ways. In carefully designed plasmid constructions, the DNA recognition site for type IIS enzymes can be removed, allowing the ligated final product to be tolerant of the endonuclease that created the overhangs (Lebedenko et al., 1991). This method is more flexible than those using conventional type II endonucleases, because the joint sequence can be designed freely. Another advantage is that the cleavage site does not have to be palindromic, thus preventing undesired homo-ligation between inserts or vectors. We reasoned that, with these features, it might be possible to have both ligation and endonuclease digestion occur simultaneously in the same tube.

As shown in Fig. 1A, all the terminals of the DNA fragments in FASTR carry cleavage sites for type IIS endonuclease followed by recognition sites for the endonuclease. The recognition sites are always outside of the cleavage sites, so after digestion by type IIS endonuclease, no recognition site remains on the DNA fragment. Because both the endonuclease and the ligase are present in the reaction mixture, equilibrium between digestion and ligation is achieved, as long as the ligated product carries the recognition site for the endonuclease. Once ligation between the designated DNA fragments is completed, there is no more digestion even in the presence of the endonuclease, because of the loss of the recognition site. It is this directional reaction that drives the designated products out of the equilibrium, enabling the recombination reaction in a single step (Fig. 1C). The sequence of the cleavage site is independent of the recognition site, allowing the terminus of each DNA fragment to have a specific sticky end for a specific partner fragment. If a three-nucleotide sticky end is used for FASTR, one can theoretically use 4^3, or 64, specific sticky ends, enabling multiple-fragment ligations (Fig. 1B).

3.2. FASTR reaction using gel-purified DNA fragments

To demonstrate this single-step recombination reaction, we amplified both the insert and vector fragments by PCR using pairs of primers with specific cleavage and recognition sites on each end. The amplified fragments were gel-extracted and mixed with type IIS endonuclease (LguI) and T4 DNA ligase. After 2 h of incubation at room temperature, 5 μl of the reaction mixture was used directly to transform chemically competent *E. coli*. To our surprise, eight samples from eight colonies gave positive results for both single- and double-fragment insertions (Fig. 2A). DNA sequencing confirmed that the sequences of the joint region were exactly as designed, verifying the validity of the FASTR reaction (Fig. 2B).

3.3. FASTR reaction using crude PCR products

Encouraged by the result, we thought it might be possible to recombine crude PCR products in a single step. In our early attempts to use this single-tube method, only few positive colonies were obtained (data not shown). We reasoned that the residual activity of the thermostable DNA polymerase would convert the sticky ends to blunt ends, giving rise to self-ligation of the vector plasmid. If so, a DNA polymerase inhibitor might help to reduce the unwanted self-ligation.

Aphidicolin has been known to inhibit the alpha subtype of DNA polymerase in eukaryotes, as well as some types of archaeal DNA polymerases (Ikegami et al., 1978; Klimczak et al., 1985). The KOD-plus DNA polymerase was derived from archaeal *Pyrococcus kodakaraensis* (Takagi et al., 1997). We therefore hypothesized that aphidicolin could inhibit the residual activity of the KOD-plus DNA polymerase present in the PCR product solution, thus allowing a higher recombination rate in the following FASTR reaction. To test the hypothesis, aphidicolin at a final concentration of 2.5 mM was added to the PCR product solution, and 1 μl each of the insert (cyan fluorescent protein, mSECFP) and vector (pRSET B) with the LguI site mutated) solutions were mixed with LguI restriction endonuclease and T4 DNA ligase. DpnI was also included in the reaction to digest the residual template DNA. After vari-

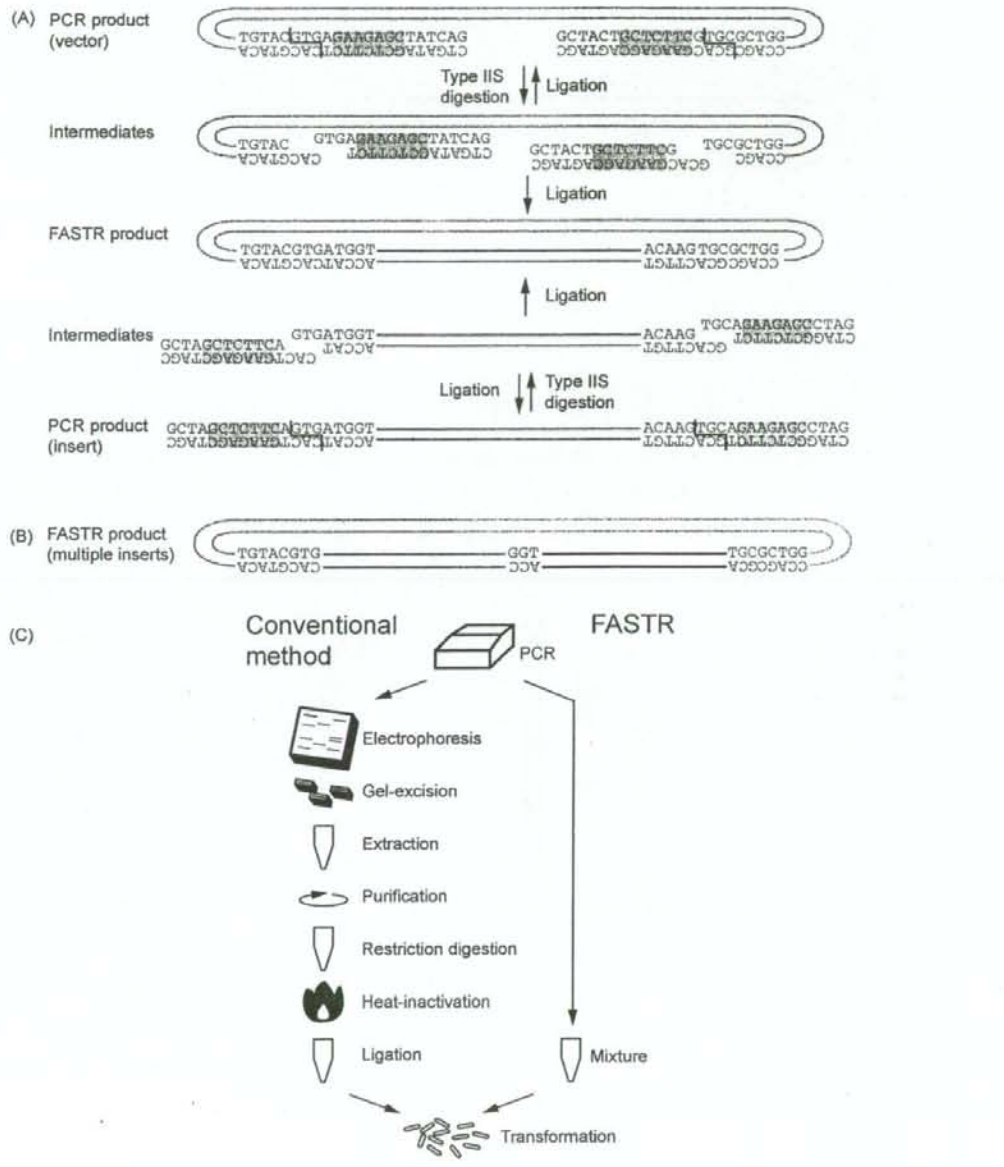

Fig. 1. Schematic representation of the FASTR reactions. (A) PCR products (top and bottom) are treated with both type IIS endonuclease and DNA ligase to induce equilibrium reactions of digestion and ligation. Once the FASTR product is assembled (middle), the reaction stops, because the final product lacks the recognition site for the endonuclease. Blue boxes represent the recognition site for type IIS endonuclease and red lines are the cleavage site of the endonuclease. Vector DNA is in orange and insert DNA is in green. (B) An example of FASTR product with multiple inserts. The inserts are indicated in green and purple. (C) Outline of the FASTR protocol. The entire procedure of FASTR is carried out in a single tube and takes less than 15 min.

ous incubation times at room temperature, JM109 DE3 competent cells were transformed with 5 μl of the FASTR reactant. With 15 min of FASTR reaction at room temperature, more than half of the colonies were fluorescent upon illumination of the plate by 470 nm blue LED. The recombination efficiency reached close to 80% when the incubation time was extended to 2 h (Fig. 2C and D).

3.4. Multiple DNA fragment assembly by FASTR reactions

We next examined the possibility of performing multiple-fragment FASTR with the crude PCR products. The procedures were essentially the same as for single-fragment FASTR, except that the joint sequences were designed so that the insertion fragments would be fused in the correct direction and order

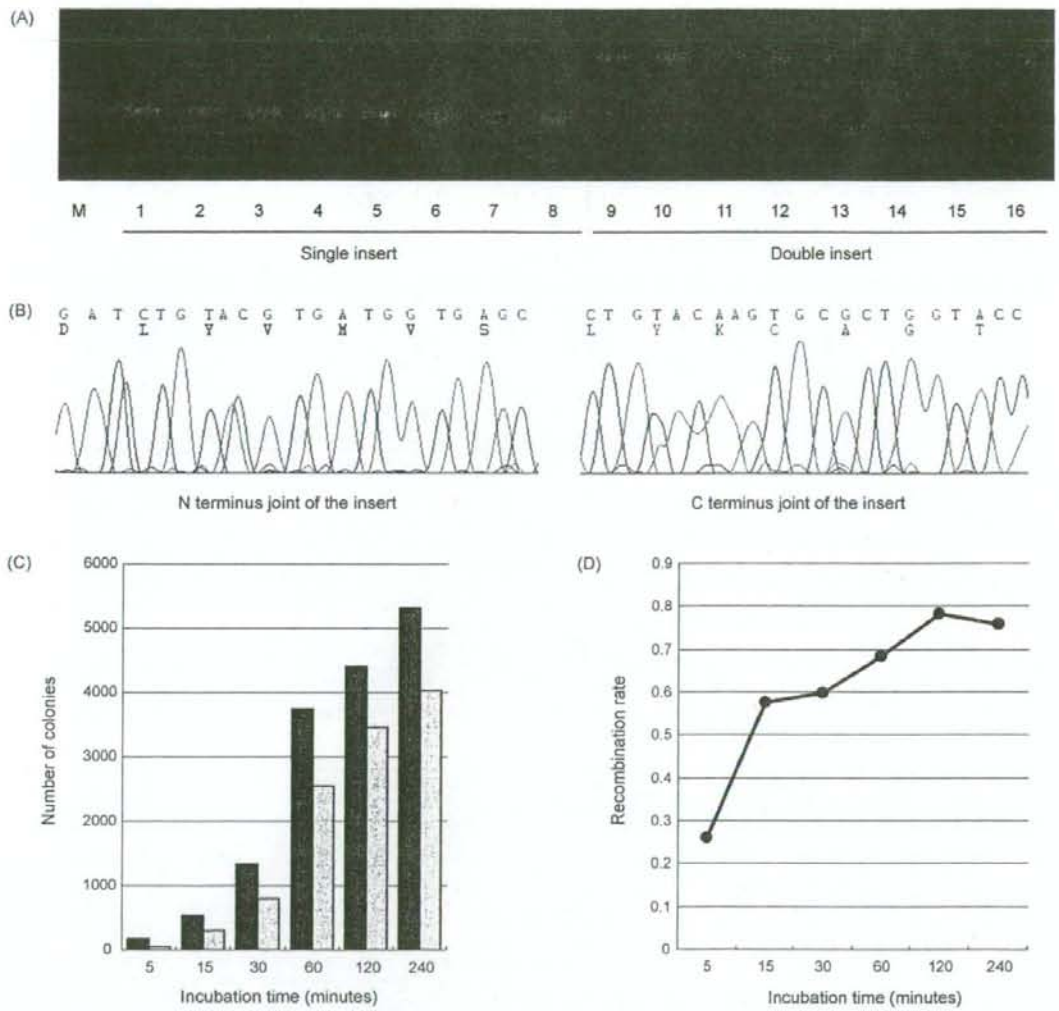

Fig. 2. High recombination rate of FASTR. *E. coli* colonies were obtained by the transformation of FASTR products. The colonies were subjected to colony PCR for insert analysis. (A) Eight randomly picked colonies were positive for single and double insertions. (B) The joints between the vector and insert were DNA sequenced to confirm the validity of the method. The FASTR reaction was carried out for various lengths of time. The number of transformed colonies reached near-plateau at 60 min (C); however, the recombination rate changed little after 15 min (D). Black bars represent the total number of colonies, and gray bars represent the number of fluorescent colonies. The recombination rate was calculated by dividing the number of fluorescent colonies by the total number of colonies.

(Fig. 1B). We amplified the insert fragments of cyan fluorescent protein (mSECFP), yellow fluorescent protein (mVenus), and red fluorescent protein (mCherry) along with the vector fragment of pRSET B. The fragments were then mixed to assemble pRSET–mSECFP–mVenus and pRSET–mSECFP–mVenus–mCherry constructs. The FASTR reaction was performed at room temperature for 1 h. We confirmed that close to half of the fluorescent colonies were double positive for mSECFP and mVenus fluorescence in pRSET–mSECFP–mVenus construct, and around 20% were triple positive for mSECFP, mVenus, and mCherry fluorescence in pRSET–mSECFP–mVenus–mCherry sample (Table 1 and Fig. 3A). These colonies were further analyzed by colony PCR to confirm the inserts (Fig. 3B).

3.5. High-throughput screening of a high-performance FRET probe by FASTR

To demonstrate the feasibility of FASTR in a practical application, we constructed a GFP-based Förster resonance energy transfer

Table 1

Insert	Number of positive colonies	Number of fluorescent colonies	Recombination rate (%)
CFP+Venus	517	1050	49.24
CFP+Venus+mCherry	50	242	20.66

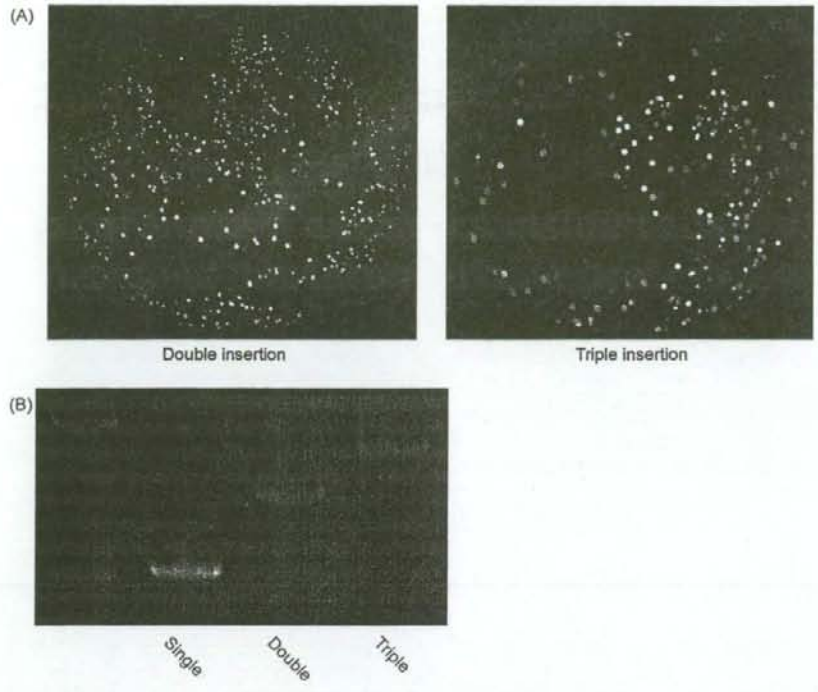

Fig. 3. Double and triple insertion by FASTR. (A) Fluorescent images of colonies expressing mSECFP, Venus, and/or mCherry were taken with multiple filter sets. The images from different color channels were overlaid and pseudocolored. Yellow colonies in the double insertion and white colonies in the triple insertion images are double and triple positives, respectively. (B) Insert lengths of the positive colonies selected by fluorescence were confirmed by colony PCR.

(FRET) pair with various linker regions to maximize FRET efficiency. FRET-based GFP probes have been widely used in biological studies as a genetically encoded molecular sensor (Piston and Kremers, 2007). One obstacle to the technology is that FRET efficiency changes dramatically with very small changes in the distance and relative orientation between fluorophores (Lakowicz, 2006). The sensitivity of a FRET pair is so acute that even a single amino-acid insertion or deletion in the linker region is enough to affect the FRET efficiency. Thus, the construction of a FRET pair requires laborious linker optimization by trial and error (Nagai and Miyawaki, 2004).

Here, we used FASTR to fuse a UV-excitable green fluorescent protein (T-Sapphire) (Zapata-Hommer and Griesbeck, 2003) to Venus, with various linker lengths between them (Fig. 4A). Thirteen reverse primers were designed for C-terminal deletion mutants of Venus, and seven forward primers for N-terminal T-Sapphire deletions. A total of 20 deletion mutants were PCR-amplified. Then 1 μl of the crude PCR products from each sample were mixed in one tube along with FASTR reagents. The FASTR reaction should recombine two inserts and a vector with correct order but in random combinations, giving rise to a total of 91 mutant combinations. After 2 h of incubation at room temperature, JM109 competent cells were transformed with 10 μl of the reactant. *E. coli* plates were screened for yellowish fluorescent colonies using a 405 nm light source. DNA sequencing of the linker region and spectroscopic analysis of the expressed proteins identified the clones with high FRET efficiency (Fig. 4B). The FRET efficiency of the best clone we obtained was determined to be 67% by cleaving the linker region (Fig. 4C), demonstrating that FASTR is an ideal method for creating a large number of multiple-fragment constructs for high-throughput screening.

4. Discussion

Although cloning techniques with type IIS restriction endonucleases and DNA ligases have been widely used, the endonuclease-mediated single-step recombination in our method is much faster than previous approaches. As far as we know, this is the first report which describes the spontaneous and directional single-tube recombination with a type IIS restriction endonuclease and DNA ligase. The reaction allows highly efficient DNA recombination, while keeping a high flexibility of class IIS restriction enzymes. Another advantage of our approach is the ability to directly recombine crude PCR products. This was made possible by adding an archeal DNA polymerase inhibitor to the FASTR reaction. Although we have not tried a monoclonal antibody against the polymerase, it might also be used to inactivate the residual polymerase activity, as it is for hot-start PCR (Kellogg et al., 1994). DpnI was also included in the reaction to selectively digest the bacterially expressed template DNA in the crude PCR products.

We primarily focused our efforts on improving the rapidity of the method, because we thought that raising the speed limit for DNA recombination would enhance research in many fields, especially ones involving high-throughput analysis. One such field is the development of GFP-based FRET probes, which are now indispensable in the biological sciences. A typical FRET probe has fluorescent donor and acceptor domains along with a sensor domain to detect biological signals. High FRET efficiency is achieved only when the distance between fluorophores is comparable to the Förster distance, and the relative dipole moments of the fluorophores are parallel to each other. The distance between fluorophores is largely affected by the linker sequences between

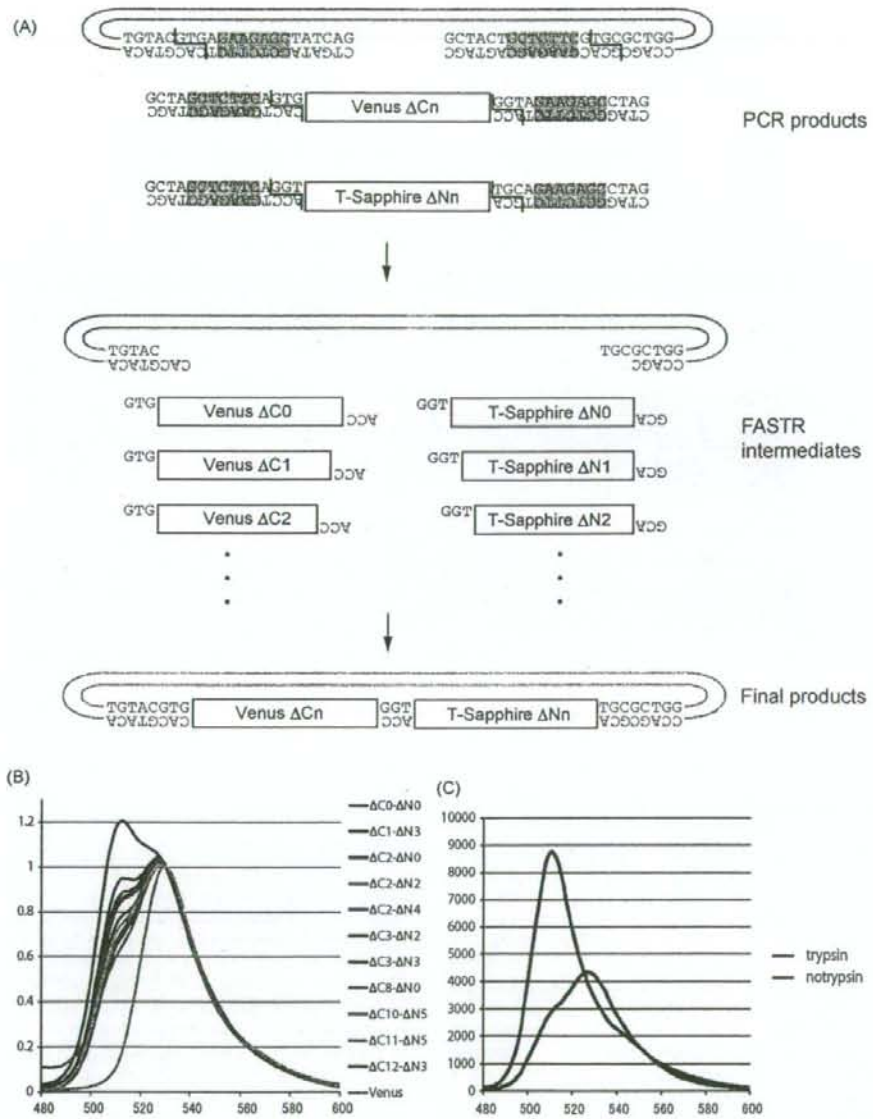

Fig. 4. Optimization of a GFP-based FRET pair. (A) A schematic representation of FRET pair optimization by FASTR. GFP variants with various lengths of linker regions are PCR-amplified (top). FASTR intermediates are indicated in the middle panel. The final products are represented in the bottom panel. An N-terminal deletion is indicated as ΔN1 and a C-terminal deletion as ΔC1. 'n' deletions are represented as ΔNn or ΔCn. (B) Fluorescence spectra of Venus (511 nm) and T-Sapphire (527 nm) fusion proteins with various linker regions. The spectra were obtained by 395 nm illumination and fluorescence scanning with a 5 nm slit. The curves were normalized to the fluorescence intensity at 530 nm. (C) Venus-T-sapphire (ΔC2–ΔN0) fusion protein was cleaved into separate fluorophores by trypsin. The FRET efficiency of the pair was calculated by fluorescence recovery of the donor protein (T-sapphire).

the domains, and the relative orientation of the fluorophores can be changed by using circular permutations of the fluorescent proteins (Nagai et al., 2004). Since it is very difficult to predict the structural state of the fluorophores by calculation, one has to optimize these parameters through empirical methods. FASTR technology can contribute to the development of such probes, because it can assemble multiple domains of FRET probes simultaneously, saving the time and cost of constructing numerous combinations of linkers and domains to obtain a favorable FRET signal.

A possible drawback of FASTR methodology would be the requirement of primers for each FASTR reaction. Although the cost and availability of synthetic oligonucleotides have been greatly improved, the requirement might be an obstacle to some researchers. Another drawback would be the imcompatibility of FASTR products with conventional restriction enzymes; the liga-

tion site of the FASTR products cannot be recut with conventional restriction enzymes. We recommend another round of FASTR reaction for an additional plasmid modification, and colony PCR for insert check.

FASTR technology is among the quickest in the latest generation of recombinant technologies, while it achieves the high efficiency of recombination-based methods and the flexibility of conventional cloning. These advantages should be applicable to most DNA manipulation procedures, including high-throughput DNA manipulations, where significant savings in time and cost are expected.

Acknowledgments

We are thankful to R.Y. Tsien for the gift of mCherry plasmid. We also thank Wataru Tomosugi for the construction of T-Sapphire plasmid, by mutating EGFP plasmid according to the published data. This work was partly supported by grants from Scientific Research on Advanced Medical Technology of the Labor, Health and Welfare of Japan to T.N., the Japanese Ministry of Education, Science and Technology to T.N., and Precursory Research for Embryonic Science and Technology (PRESTO) of the Japan Science and Technology Agency (JST) to I.K.

References

Hartley, J.L., Temple, G.F., Brasch, M.A., 2000. DNA cloning using in vitro site-specific recombination. Genome Res. 10, 1788–1795.

Ikegami, S., Taguchi, T., Ohashi, M., Oguro, M., Nagano, H., Mano, Y., 1978. Aphidicolin prevents mitotic cell division by interfering with the activity of DNA polymerase-alpha. Nature 275, 458–460.

Kellogg, D.E., Rybalkin, I., Chen, S., Mukhamedova, N., Vlasik, T., Siebert, P.D., Chenchik, A., 1994. TaqStart antibody: "hot start" PCR facilitated by a neutralizing monoclonal antibody directed against Taq DNA POLYMERASE. Biotechniques 16, 1134–1137.

Kleid, D., Humayun, Z., Jeffrey, A., Ptashne, M., 1976. Novel properties of a restriction endonuclease isolated from *Haemophilus parahaemolyticus*. Proc. Natl. Acad. Sci. U.S.A. 73, 293–297.

Klimczak, L.J., Grummt, F., Burger, K.J., 1985. Purification and characterization of DNA polymerase from the archaebacterium *Sulfolobus acidocaldarius*. Nucleic Acids Res. 13, 5269–5282.

Lakowicz, J.R., 2006. Principles of Fluorescence Spectroscopy. Springer, New York, pp. 443–475.

Lebedenko, E.N., Birikh, K.R., Plutalov, O.V., Berlin Yu, A., 1991. Method of artificial DNA splicing by directed ligation (SDL). Nucleic Acids Res. 19, 6757–6761.

Liu, Q., Li, M.Z., Leibham, D., Cortez, D., Elledge, S.J., 1998. The univector plasmid-fusion system, a method for rapid construction of recombinant DNA without restriction enzymes. Curr. Biol. 8, 1300–1309.

Matsuda, T., Miyawaki, A., Nagai, T., 2008. Direct measurement of protein dynamics inside cells using a rationally designed photoconvertible protein. Nat. Methods 5, 339–345.

Nagai, T., Miyawaki, A., 2004. A high-throughput method for development of FRET-based indicators for proteolysis. Biochem. Biophys. Res. Commun. 319, 72–77.

Nagai, T., Ibata, K., Park, E.S., Kubota, M., Mikoshiba, K., Miyawaki, A., 2002. A variant of yellow fluorescent protein with fast and efficient maturation for cell-biological applications. Nat. Biotechnol. 20, 87–90.

Nagai, T., Yamada, S., Tominaga, T., Ichikawa, M., Miyawaki, A., 2004. Expanded dynamic range of fluorescent indicators for Ca^{2+} by circularly permuted yellow fluorescent proteins. Proc. Natl. Acad. Sci. U.S.A. 101, 10554–10559.

Piston, D.W., Kremers, G.J., 2007. Fluorescent protein FRET: the good, the bad and the ugly. Trends Biochem. Sci. 32, 407–414.

Podhajska, A.J., Szybalski, W., 1985. Conversion of the FokI endonuclease to a universal restriction enzyme: cleavage of phage M13mp7 DNA at predetermined sites. Gene 40, 175–182.

Shu, X., Shaner, N.C., Yarbrough, C.A., Tsien, R.Y., Remington, S.J., 2006. Novel chromophores and buried charges control color in mFruits. Biochemistry 45, 9639–9647.

Szybalski, W., Kim, S.C., Hasan, N., Podhajska, A.J., 1991. Class-IIS restriction enzymes—a review. Gene 100, 13–26.

Takagi, M., Nishioka, M., Kakihara, H., Kitabayashi, M., Inoue, H., Kawakami, B., Oka, M., Imanaka, T., 1997. Characterization of DNA polymerase from Pyrococcus sp. strain KOD1 and its application to PCR. Appl. Environ. Microbiol. 63, 4504–4510.

Takemori, H., Katoh, Y., Horike, N., Doi, J., Okamoto, M., 2002. ACTH-induced nucleocytoplasmic translocation of salt-inducible kinase Implication in the protein kinase A-activated gene transcription in mouse adrenocortical tumor cells. J. Biol. Chem. 277, 42334–42343.

Zacharias, D.A., Violin, J.D., Newton, A.C., Tsien, R.Y., 2002. Partitioning of lipid-modified monomeric GFPs into membrane microdomains of live cells. Science 296, 913–916.

Zapata-Hommer, O., Griesbeck, O., 2003. Efficiently folding and circularly permuted variants of the Sapphire mutant of GFP. BMC Biotechnol. 3, 5.

Direct measurement of protein dynamics inside cells using a rationally designed photoconvertible protein

Tomoki Matsuda[1], Atsushi Miyawaki[2] & Takeharu Nagai[1]

All biological reactions depend on the diffusion and re-localization of biomolecules. Our understanding of biological processes requires accurate measurement of biomolecule mobility in living cells. Currently, approaches for investigating the mobility of biomolecules are generally restricted to measuring either fast or slow diffusion kinetics. We describe the development and application of a photoconvertible fluorescent protein, Phamret, that can be highlighted by UV light stimulation inducing a change in fluorescence emission from cyan fluorescent protein (CFP) to photoactivated GFP (PA-GFP). Phamret can be monitored by single excitation-dual emission mode for visualization of molecular dynamics for a broad range of kinetics. We also devised a microscopy-based method to measure the diffusion coefficient from the fluorescence decay after photostimulation of Phamret, enabling analysis of diffusion kinetics ranging from less than 0.1 $\mu m^2/s$ up to ~100 $\mu m^2/s$, and found significant changes in free protein movement during cell-cycle progression.

Application of GFP and related fluorescent proteins has revolutionized our ability to analyze a wide range of biological processes such as gene expression, protein localization and cell motility in living specimens. Advances in fluorescence microscopy techniques have also enabled higher-resolution imaging of the fluorescence signals from fluorescent protein fusion constructs, providing insights into the movement of biomolecules and their interactions with cellular components[1,2].

Among these methods, imaging fluorescence resonance energy transfer (FRET) between two fluorescent proteins provides spatiotemporal information of protein-protein interactions and protein conformational changes in living cells[3]. FRET is the radiation-less energy transfer from an excited donor to an acceptor fluorophore that occurs when both molecules are in close proximity within ~10 nm at an appropriate orientation of the dipole moment. This technology has been used to develop genetically encoded fluorescent indicators for various cellular events[3].

Several microscopy techniques, including fluorescence correlation spectroscopy (FCS) and fluorescence recovery after photobleaching (FRAP), are used to investigate mobility of biomolecules in living cells. FCS is used to determine the diffusion coefficient and the concentration of biomolecules in live cells by monitoring fluctuations in fluorescence intensity in a diffraction-limited spot of a laser beam[4]. FRAP is also used to investigate protein dynamics by photobleaching fluorescent molecules using a high-powered laser and then recording the movement of surrounding non-bleached fluorescent molecules into the photobleached area[5]. From the recovery curve, it is possible to estimate both the diffusion coefficient and immobile fraction of the tested proteins[6].

In recent years, various photosensitive fluorescent proteins have been developed by engineering existing fluorescent proteins or cloning new proteins from fluorescent organisms[7]. These photosensitive fluorescent proteins provide means to optically highlight selected proteins and to measure protein dynamics. Photosensitive fluorescent proteins can be classified into two types: photoactivatable and photoconvertible fluorescent proteins. Photoactivatable fluorescent proteins are those that are reversibly or irreversibly changed from a dark state to a bright state by photostimulation, such as PA-GFP[8], photoactivatable mRFP1 (ref. 9), KFP1 (ref. 10) and Dronpa[11]. In contrast, photoconvertible fluorescent proteins maintain a bright state but undergo an emission wavelength change from the pre- to post-photoconversion state by photostimulation. Examples of photoconvertible fluorescent proteins are Kaede[12], mEosFP[13], PS-CFP[14], KikGR[15] and Dendra[16]. The ability to detect both pre- and post-photoconversion states is a preferred characteristic for live-cell imaging, but all presently available photoconvertible fluorescent proteins undergo a change in excitation wavelength in addition to the shift in emission wavelength. This therefore requires a complicated microscope setup and also makes it difficult to measure rapid molecular dynamics. Furthermore, photoconvertible fluorescent proteins except PS-CFP, mEosFP and Dendra function as oligomers, which hinders their use as protein tags.

To overcome these problems, we rationally designed a monomeric photoconvertible fluorescent protein, Phamret, that requires only one wavelength to excite both the pre- and post-photoconverted states, thus enabling quantitative observation of rapidly diffusible molecules. We also developed a microscopy method, FDAP, for measurement of rapid diffusion of molecules, up to ~100 $\mu m^2/s$ using Phamret or other photosensitive

[1]Laboratory for Nanosystems Physiology, Research Institute for Electronic Science, Hokkaido University, Kita-12 Nishi-6 Kita-ku, Sapporo, Hokkaido, 060-0812, Japan. [2]Laboratory for Cell Function and Dynamics, Brain Science Institute, RIKEN, 2-1 Hirosawa, Wako, Saitama, 351-0198, Japan. Correspondence should be addressed to T.N. (tnagai@es.hokudai.ac.jp).

RECEIVED 2 JANUARY; ACCEPTED 14 FEBRUARY; PUBLISHED ONLINE 16 MARCH 2008; DOI:10.1038/NMETH.1193

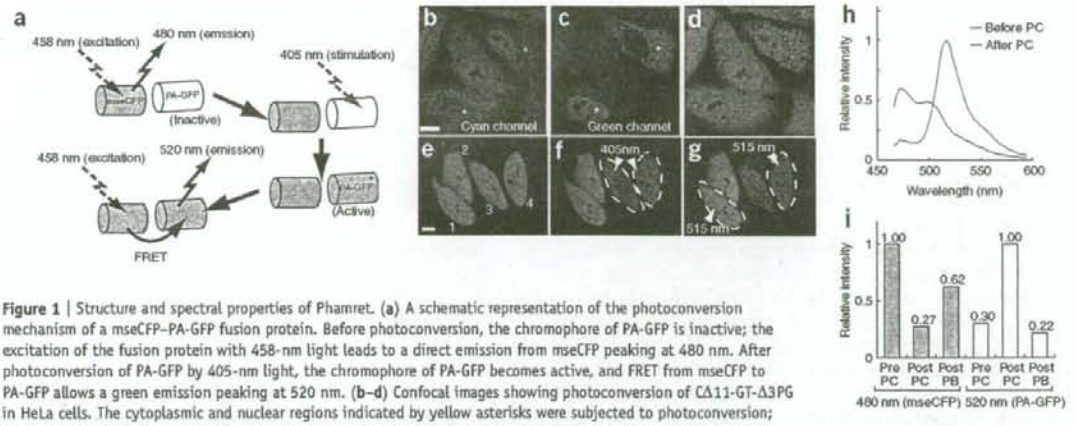

Figure 1 | Structure and spectral properties of Phamret. (**a**) A schematic representation of the photoconversion mechanism of a mseCFP–PA-GFP fusion protein. Before photoconversion, the chromophore of PA-GFP is inactive; the excitation of the fusion protein with 458-nm light leads to a direct emission from mseCFP peaking at 480 nm. After photoconversion of PA-GFP by 405-nm light, the chromophore of PA-GFP becomes active, and FRET from mseCFP to PA-GFP allows a green emission peaking at 520 nm. (**b–d**) Confocal images showing photoconversion of CΔ11-GT-Δ3PG in HeLa cells. The cytoplasmic and nuclear regions indicated by yellow asterisks were subjected to photoconversion; the images for both the cyan (465–510 nm; **b**) and green (510–600 nm; **c**) fluorescence were taken. The images of mseCFP and PA-GFP were pseudocolored (cyan and red, respectively) and superimposed (**d**). (**e–g**) Pseudocolored images of CΔ11-GT-Δ3PG–expressing HeLa cells before photoconversion (**e**), after photoconversion (**f**) and after photobleaching (**g**). The regions surrounded by dashed yellow circles in **f** and **g** were photoconverted by 405-nm light stimulation and photobleached by 515-nm intense laser irradiation, respectively. Scale bars, 10 μm. (**h**) Emission spectra of Phamret in HeLa cells before and after photoconversion (PC). (**i**) Relative fluorescence intensity of mseCFP and PA-GFP before photoconversion (Pre PC), after photoconversion (Post PC) and after photobleaching (Post PB).

fluorescent proteins. The characteristic features of this method are (i) quick photostimulation time (0.25 ms); (ii) small light energy necessary for photostimulation (<1 W/cm^2 in case of Phamret); (iii) fast acquisition of fluorescence decay (4,100 Hz) by reciprocal line scanning; and (iv) consideration of photobleaching during fluorescence decay measurement.

RESULTS

Design and evaluation of Phamret

To develop a photoconvertible fluorescent protein that can be excited by the same wavelength in both pre- and post-photoconversion states, we designed a fusion protein composed of a CFP variant (mseCFP) fused to a PA-GFP[8] (**Fig. 1a**). We designed this fusion protein to emit cyan fluorescence (480 nm) in the pre-photoconverted state, which can be shifted to green fluorescence (520 nm) by UV light stimulation of PA-GFP into a FRET acceptor for the mseCFP donor (**Fig. 1a**). This approach requires a high FRET efficiency between mseCFP and activated PA-GFP; otherwise no or small changes in fluorescence emission can be observed after UV stimulation. To achieve a high FRET efficiency, we concatenated mseCFP containing a C-terminal 11-amino-acid truncation to PA-GFP with a 3-amino-acid truncation from the N terminus via a dipeptide (Gly-Thr) linker. The bacterially expressed chimeric protein (CΔ11-GT-Δ3PG) exhibited a fivefold increase in the emission ratio (520 nm/480 nm) upon brief photoactivation by 420-nm pulsed laser. When expressed in living mammalian cells, CΔ11-GT-Δ3PG was distributed uniformly in both the cytoplasm and the nuclei (**Fig. 1b–d**). Spectral imaging revealed that all fluorescent cells had an emission spectrum identical to that of mseCFP, whereas upon 405-nm laser stimulation, the fluorescence emission in the stimulated area quickly changed from cyan to green, indicative of complete maturation of both mseCFP and PA-GFP in CΔ11-GT-Δ3PG at 37 °C (**Fig. 1e–g** and **Supplementary Fig. 1a–f** online). Upon activation, green fluorescence increased 3.3-fold, and cyan fluorescence emission decreased 3.7-fold, resulting in an approximately 12.2-fold ratio change between the pre- and post-photoconverted states (**Fig. 1h,i**). To confirm that the photoconversion of CΔ11-GT-Δ3PG was indeed due to FRET from mseCFP to activated PA-GFP, we bleached the acceptor PA-GFP. The decrease in PA-GFP emission peak was accompanied by dequenching of the mseCFP signal (**Fig. 1g–i** and **Supplementary Fig. 1g–i**), demonstrating that the dominant mechanism of the fluorescence color change in CΔ11-GT-Δ3PG was caused by FRET between mseCFP and activated PA-GFP. Therefore, we named this fusion protein Phamret for photoactivation-mediated resonance energy transfer. The photoconversion of Phamret was achieved using a lower laser power density (<1 W/cm^2) than that for photobleaching. Accordingly, the quantum yield for photoconversion of Phamret was 2.7×10^{-2}, which was five times greater than that for the efficient highlighter, KikGR[15] (4.7×10^{-3}). pH titration of Phamret revealed that a high dynamic range (>10-fold) was achieved in a neutral to alkaline environment ($>$pH 7), but it was strongly attenuated at acidic pH (**Supplementary Fig. 2a** online) and displayed a twofold dynamic range at pH 6.5. Phamret thus functions as a highlighter at physiological pH ranging from 6.5 to 8.0. Phamret was estimated to be a 53.4-kDa protein and is monomeric in living cells without displaying any unexpected binding to protein or proteolytic digestion (**Supplementary Fig. 2b–d**). Concordantly, Phamret in fusion with human β-actin and fibrillarin as well as targeting sequences for the Golgi bodies and the peroxisome showed an expected localization pattern (**Fig. 2a–d**) as reported previously[17–20]. In addition, the fusion proteins did not substantially perturb cellular functions such as cell division. Furthermore, all the fusion proteins tested underwent pronounced photoconversion by 405-nm laser illumination (**Fig. 2a–d**). Although we successfully labeled most of the proteins tested with Phamret, labeling of α-tubulin was unsuccessful (data not shown). Optimization of the amino-acid linker sequence and length between Phamret

and the protein of interest may resolve this problem. The properties of Phamret in comparison with other photoconvertible fluorescent proteins developed so far are shown in **Table 1**.

Cellular application of Phamret

To demonstrate the applicability of Phamret to stably label the intracellular structures, we expressed Phamret in mitochondria and took time-lapse images after Phamret photoconversion in one region. During a 15-min recording, a long thread-like mitochondrion fused and divided frequently, dramatically changing the pattern of the mitochondria network (**Fig. 2e–h** and **Supplementary Video 1** online). In parallel with the changes in the mitochondria structure, the shifted fluorescence color in the photoconverted region spread out and entered a surrounding mitochondrion. In addition, the labeled region in the fused mitochondrion was exchanged until it came to equilibrium at the intermediate color, indicating conjugation of the mitochondrial matrix and diffusion of the material in the fused mitochondrion.

We also observed positioning of chromosomes during mitosis in living mammalian cells. We labeled chromosomes in HeLa cells by expressing a histone 2B–Phamret fusion protein (H2B-Phamret). Owing to the very low dissociation rate of H2B from chromatin[21], the photoconverted marking remained detectable for many hours, allowing imaging of the dynamics of labeled chromosomes[22]. Just before mitosis, we photoconverted the nuclear halves and performed time-lapse imaging. In most cells (82%, $n = 14$), the global pattern of the mother cells was transmitted to the two daughter nuclei in G1 phase in a mirror-symmetric fashion (**Fig. 2i,j** and **Supplementary Video 2** online), indicating the heritability of chromosomal positions during cell division as previously shown by FRAP analysis using fluorescent protein tags in normal rat kidney cells[22].

Visualization of rapid protein dynamics using Phamret

All photoconvertible fluorescent proteins described to date undergo a change in excitation wavelength in addition to the shift in

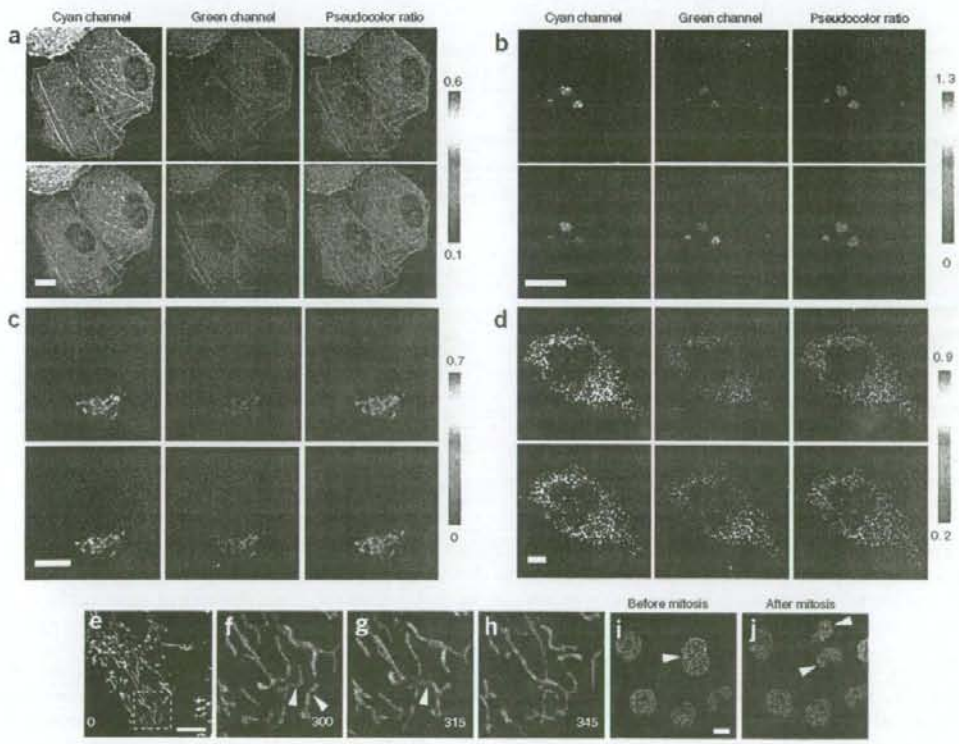

Figure 2 | Photoconversion of Phamret fusion protein in living cells. (**a–d**) Confocal fluorescence images of HeLa cells expressing Phamret fused to actin (**a**), fibrillarin (**b**), Golgi body localizing signal (**c**) and SKL tripeptide for peroxisome localization (**d**) before photoconversion (top) and after photoconversion (bottom) in the selected area, as shown in red (bottom right). The cyan channel, green channel and pseudocolored emission ratio (green to cyan) images are shown. Color bars represent green-to-cyan intensity ratio. (**e–h**) To track mitochondria, Phamret-expressing mitochondria in the selected area (as shown in red in **e**) were subjected to photoconversion (**e**). A yellow dashed box in **e** shows the region used for time-lapse imaging. Representative images taken at 300 s (**f**), 315 s (**g**) and 345 s (**h**) after photoconversion are shown. The yellow and white arrowheads in **f** indicate two mitochondria that were about to fuse. Arrowhead in **g** indicates the point of mitochondrial fusion, which was followed by spreading of Phamret protein in the fused mitochondrion (**h**). (**i,j**) Tracking of H2B-Phamret during mitosis. Half of the nucleus (arrowhead) being photoconverted just before mitosis (red; **i**). The daughter nuclei (arrowheads) show the preserved color pattern (**j**). Scale bars, 10 μm.

Table 1 | Properties of known photoconvertible proteins

Protein	Fluorescence color: Before photoconversion / After photoconversion	Observed wavelength[a] (nm): Excitation	Observed wavelength[a] (nm): Emission	Stimulation: Wavelength (nm)	Stimulation: Power density (W/cm^2)	Fluorescence increase in ratio	Oligomeric status	Ref.
Phamret	Cyan	458	475	405	$<1^b$ ($\Phi_{PC} = 2.7 \times 10^{-2}$)[b]	~15[b]	Monomer	
	Green	458	517					
PS-CFP	Cyan	435	468	405	5–10	~1,500	Monomer	14
	Green	490	511					
Kaede	Green	488	518	405	1.3	~2,000	Tetramer	12
	Red	543	580					
KikGR	Green	488	517	405	~1 ($\Phi_{PC} = 4.7 \times 10^{-3}$)	NS	Tetramer	15
	Red	543	593					
EosFP	Green	488	516	405	NS	NS	Tetramer	13
	Red	543	581					
d2EosFP	Green	488	516	405	500	NS	Dimer	13
	Red	543	581					
mEosFP	Green	488	516	405	NS	NS	Monomer	13
	Red	543	581					
Dendra	Green	488	505	488	1.5	~1,500–4,500	Monomer	16
	Red	543	575	405	0.6			
Cy11.5	Yellow	440	527	515 (bleaching)	$>10^b$	NS	Monomer	28
	Cyan	440	476					

Φ_{PC}, quantum yield for photoconversion. NS, not stated.
[a]Wavelength of excitation light for live imaging by microscopy and peak of emission spectrum. [b]Measured in our laboratory. A laser power meter was used to measure total power of the light after the objective lens. Light power density was estimated by dividing the total power by the area of the illuminated region.

emission wavelength upon photoconversion, and thus require measurement in dual excitation–dual emission mode. Generally, two different excitation wavelengths are alternated to obtain images both before and after photoconversion. This is unfavorable for observing rapidly diffusing molecules because of the acquisition time lag between two images. Even if we excite simultaneously the two states of photoconvertible fluorescent proteins, it is impractical because two lasers must be aligned to the same confocal spot by bringing two laser beams to a perfect and stable overlap. The single excitation property of Phamret overcomes this problem, but it may be possible to measure the presently available dual-excitation photoconvertible fluorescent proteins in single-excitation mode also. To address this, we compared the photoconversion contrast of Phamret with the dual-excitation photoconvertible fluorescent proteins, tandem dimer Dendra (td-Dendra), which is comparable in size to Phamret[16]. We expressed both proteins in HeLa cells, photoconverted them by 405-nm laser irradiation and simultaneously measured the change in fluorescence intensity of both pre- and post-photoconversion states at the frame rate of 41 Hz using an appropriate excitation wavelength for each. At the first frame image after photoconversion, Phamret showed a 1.3-fold decrease and 2.4-fold increase in cyan and green fluorescence, respectively, yielding a 3.1-fold change in the emission ratio (**Supplementary Fig. 3a** online). The slower decrease in green fluorescence may be due to the photobleaching of PA-GFP moiety in Phamret. In contrast, td-Dendra had a 1.4-fold decrease in green fluorescence and no change in red fluorescence just after photoconversion, resulting in smaller contrast than for Phamret (**Supplementary Fig. 3b**). These results indicate that when using the single excitation–dual emission mode for fast frame acquisition, Phamret promises a higher contrast than Dendra. To further evaluate this,

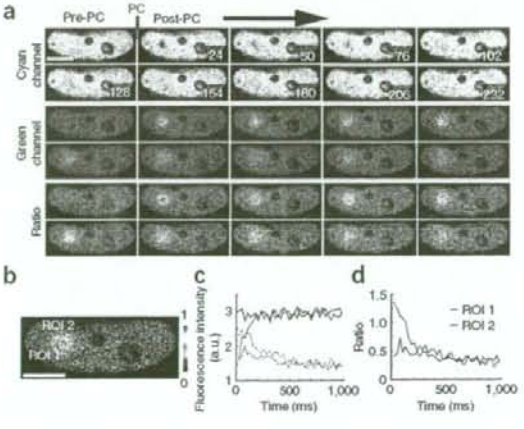

Figure 3 | Visualization of rapid protein dynamics using Phamret. (**a**) Confocal images of donor CFP (top), acceptor PA-GFP (middle) and pseudocolored emission ratio (green/cyan; bottom) showing diffusion of photoconverted PP2Cγ-Phamret. Images were taken every 26 ms. (**b**) A magnified view of the first image just after photoconversion. The white circles (diameter 1.10 μm) represent ROIs used for intensity calculation. ROI 1 was set on the photoconverted circular region (diameter 1.38 μm). ROI 2 was placed outside of the photoconverted region. Distance between the centers of two ROIs is 2.1 μm. (**c**) Time course of cyan (solid line) and green (dashed line) fluorescence intensity of Phamret in ROI 1 (red) and ROI 2 (blue). (**d**) Time course of green to cyan emission ratio in ROI 1 and ROI 2. Scale bars, 10 μm.

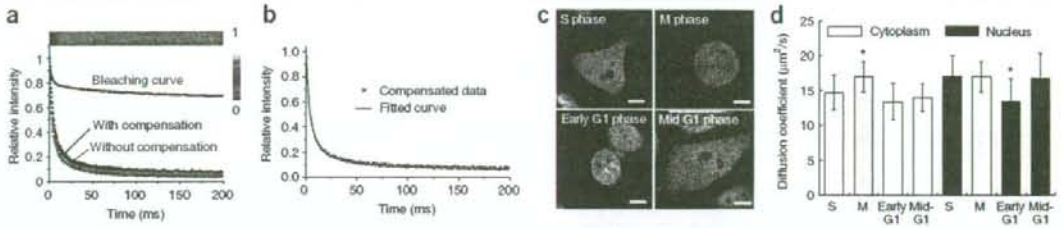

Figure 4 | Determination of diffusion coefficient of Phamret by FDAP. (**a**) Line-scanned images of photoconverted Phamret in solution were taken, and the kymographs of the images are shown in pseudocolor (top). Color bar indicates normalized fluorescence intensity. Average fluorescence decay curves in the solution were calculated (bottom). The blue curve represents the bleaching of photoconverted Phamret during image acquisition. (**b**) The compensated fluorescence decay curve determined by equation (3). (**c**) Fluorescence images of a cell at the indicated cell-cycle stages used for FDAP measurements. Scale bar, 10 μm. (**d**) Diffusion coefficient of Phamret in the cytoplasm and the nucleus at the indicated cell-cycle stages. In the case of M phase, the same data are shown (light gray bars) because the cytoplasm and nucleus cannot be distinguished due to the disappearance of the nuclear membrane. Asterisks (*) indicate the cell phase where the diffusion coefficient is significantly different from other phases in either the cytoplasm or nucleus, respectively. Error bars are s.d. ($n > 10$). Validity of the differences was statistically confirmed by one-way analysis of variance (ANOVA) and defined as significant at $P = 4.0 \times 10^{-6}$ and 4.1×10^{-4}, respectively. Differences between cytoplasm and nucleus in S and G1 phase were also confirmed by using two-sided *t*-test ($P = 0.005$ and 0.008) with significance level $\alpha = 0.05$.

we examined a PP2Cγ-Phamret fusion protein in the nucleus of a HeLa cell. After photoconversion of PP2Cγ-Phamret in a region of the nucleus, we acquired fluorescence images at 41 Hz that show how fast the photoconverted PP2Cγ-Phamret diffuses (**Fig. 3** and **Supplementary Video 3** online).

Determination of biomolecule diffusion coefficients

To determine diffusion coefficients of proteins tagged with photosensitive fluorescent proteins, we devised a new microscopy technique that enables measurement of a wide range of diffusion coefficients. This technique, FDAP, is based on measurement of fluorescence decay after photostimulation of photosensitive fluorescent proteins by quick (0.25 ms) photo-irradiation using a focused laser followed by repeated reciprocal line scanning at 4,100 Hz. We used a laser confocal microscope equipped with a dual laser scanner to carry out photostimulation during fluorescence measurement. We used Phamret as the photosensitive fluorescent protein, and measured the diffusion coefficient in aqueous solution (**Fig. 4a**). When we used averaged fluorescence decay data derived from 10 measurements directly for fitting by Eq. 3, the estimated diffusion coefficient was $70.4 \pm 0.8\ \mu m^2/s$. This value is much larger than $50.4\ \mu m^2/s$ determined by FCS for the GFP tandem dimer[23]. Because the FDAP experiment required about ten times more intense laser irradiation for excitation than that used in FRAP to acquire line images with a high-enough signal-to-noise ratio, we speculated that the difference in measured diffusion coefficients was due to photobleaching of PA-GFP moiety in Phamret during the fluorescence decay measurement (**Supplementary Fig. 3a**). To estimate the influence from photobleaching, we recorded a time course of fluorescence intensity using fully photoconverted Phamret in solution or in a cell in which we neglected the fluorescence decay caused by the molecular diffusion. Although the fluorescence attenuation rate in FDAP was larger than that expected from simple bleaching immediately after starting the measurement, the total number of bleached molecules was comparable between FDAP and FRAP at the end of measurements (**Supplementary Fig. 4a,b** online). We used the measured decay curve (**Fig. 4a**) for data compensation and applied the compensated data for nonlinear curve fitting (**Fig. 4b**). The diffusion coefficient after correction was $49.5 \pm 0.6\ \mu m^2/s$, which was almost equivalent to the previous FCS data[23]. Recently, a method to measure faster diffusion using FRAP by attempting to account for the finite time of the photobleaching has been proposed[24]. Therefore, we performed FRAP measurements to compare the results with those of FDAP (**Supplementary Fig. 4c–f**) and FCS analyses. All three methods gave comparable results for tandem fluorescent protein dimers (**Table 2**). However, the diffusion coefficient of a single fluorescent protein measured by FRAP was substantially different from those obtained by FDAP and FCS, indicating that FDAP may be more reliable than FRAP for analysis of fast-diffusing molecules with $>20\ \mu m^2/s$ diffusion coefficient, provided that an accurate bleaching curve can be obtained for correction of the FDAP data (**Table 2**).

To validate the performance of FDAP, we compared the diffusion coefficient of Phamret in HeLa cells at different stages of the cell cycle (S/G2, M, early G1 and mid-G1) as well as in different compartments, cytoplasm and nucleus (**Fig. 4c**). We obtained a correction curve for this experiment using fully photoconverted Phamret in HeLa cells. Generally, the diffusion coefficient of Phamret in the nucleus was greater than that in cytoplasm except in early-G1 phase in which Phamret in both nucleus and cytoplasm showed a similar diffusion coefficient (**Fig. 4d**). Furthermore, we found that the diffusion coefficients in the nucleus during early-G1 phase ($13.4 \pm 3.3\ \mu m^2/s$) were significantly smaller than those in other phases (17.0 ± 3.1 in S phase, 17.1 ± 2.2 in M phase, 16.8 ± 3.7 in mid-G1 phase; **Fig. 4d**). Although the cells in M phase are classified into neither cytoplasm nor nucleus because both compartments are mixed after disappearance of the nuclear membrane, the diffusion coefficient of Phamret in M phase tends to show the

Table 2 | Comparison of FDAP with other methods

Fluorescent protein	FDAP D ($\mu m^2/s$)	FRAP D ($\mu m^2/s$)	FCS D ($\mu m^2/s$)
Single	22.9 ± 3.7	34.0 ± 8.5	23.4 ± 2.5
Tandem dimer	14.1 ± 2.4	18.3 ± 6.4	16.4 ± 0.8

value for S and mid-G1 phase nucleus, suggesting that the cellular environment of the M-phase cell was more nuclear-like than cytoplasm-like.

DISCUSSION

The microscopy method we developed, FDAP, allowed reliable measurement of diffusion coefficients up to ~100 μm²/s, the measurement of which has been quite difficult using FRAP. The reason why FRAP gave a different diffusion coefficient in the comparison of FDAP and FCS, may be due to the use of the first frame image after photobleaching to calculate the bleaching constant in FRAP[24]. The first frame image after photobleaching contains irrelevant diffusion data obtained during the photobleaching and the first image acquisition. Thus, this may affect the calculation of the bleaching constant, especially for fast-diffusing molecules, resulting in an overestimation of the diffusion coefficient. According to reference 25, the total bleaching time should be at least 15 times smaller than the characteristic recovery time[25]. The photostimulation time of 0.25 ms in our FDAP measurement is brief enough that the diffusion during photostimulation can be neglected. Moreover, the FRAP measurement has other drawbacks: the bleaching constant needs to be determined whenever the target molecules or intracellular environment are changed because the value of the bleaching constant depends on the diffusion constant of the target molecules. In the presence of a highly immobile fraction, the bleaching profile in the first image contains contributions of both the diffusing mobile fraction and the stationary immobile fraction, requiring complex assumptions[24]. Our FDAP method is not affected by this issue.

Compared to FCS, FDAP has the advantage of retrieving additional information regarding the states of the immobile molecules. FDAP can be used to investigate any diffusion kinetics ranging from <0.1 μm²/s to ~100 μm²/s. Notably, when compared with FCS, measurement time for a fast diffusible protein (>10 μm²/s) by FDAP is much shorter (200 ms for FDAP versus >10 s FCS[23]), which is an advantage when analyzing molecules that quickly change diffusion coefficient upon stimulation.

In the post genomic era, many cascade maps for signal transduction pathways activated by biological events have been described. These maps are very useful for understanding the mechanisms of cellular activity at the molecular level. Information on protein and molecule movement rates within cells provides enhanced understanding of not only signal transduction but also various physiological phenomena at the molecular level. The ability to measure molecular mobility over a broad kinetic range with this single technique provides a useful complement to FRAP or FCS, thus benefiting studies on molecular dynamics in living cells.

METHODS

Imaging. For cell imaging we used an Olympus confocal inverted microscope FV1000 equipped with UPLSAPO 60× 1.35 numerical aperture (NA) oil objective and multi-Argon ion laser. We used a 405 nm laser diode for photostimulation. We acquired the cyan and green fluorescence signals by excitation at 458 nm and detected them at 465–510 nm and 510–600 nm wavelength range, respectively. For td-Dendra imaging, we simultaneously acquired the green (495–525 nm) and red fluorescence (560–650 nm) signals by excitation at 488 nm. We created the fluorescence ratio images using AquaCosmos software (Hamamatsu Photonics).

Determination of diffusion coefficient by FDAP. We estimated the activation characteristics of the laser using fixed cells expressing Phamret. First, we photoconverted Phamret in a fixed cell by the pulse irradiation with a 405-nm laser for 0.25 ms, and measured fluorescence intensity. Then we photoconverted the whole region of the same cell again until the fluorescence came to equilibrium, and again measured the fluorescence intensity. We divided the fluorescence intensity of once-photoconverted Phamret at the position (r) from the center of the activated region by the fluorescence intensity of fully photoconverted Phamret. We fitted the divided values at different positions to the Gaussian laser profile modified from the previously published one[26] so that the center of the activation profile became the peak value of fluorescence intensity as described by following equation:

$$C(r) = 1 - \exp\left(-K\exp\left(-\frac{2r^2}{w^2}\right)\right), \quad (1)$$

where $C(r)$ is the concentration of the photoconverted Phamret, K is the activation constant for the fixed cells, and w is the half-width of the laser beam at $1/e^2$ intensity.

Each FDAP experiment started with image scans, followed by a 405-nm laser irradiation for 0.25 ms on a point in the scanning area. We collected a series of line scanned images of the fluorescence emission in the region of 510–600 nm at 0.244 ms intervals (≈4,100 Hz) for 200 ms using 488-nm laser as excitation light. We skipped the first line scanning image to avoid direct influence of the irradiated pulse of the 405 nm laser. We fixed the length of line scanning to 80 pixels, and each pixel width was 103 nm. We used the central 8 pixels (0.824 μm) in the scanned line as a region of interest for the fluorescence intensity measurement. We calculated the background signals as the average intensity in the region of interest, which we measured 50 ms before photoconversion. We calculated the average fluorescence in the region of interest (ROI) at time t after the photoconversion, $I_{ROI}(t)$, from each line image with the subtracted background signal. The fluorescence signal measured in a region of interest normalized to the change in total fluorescence was determined as

$$I_{\text{rel. image}}(t) = \frac{I_{ROI}(t)}{I_{max}}, \quad (2)$$

where I_{max} is the maximum intensity after the photoconversion.

Because the measured fluorescence decay contains contribution from photobleaching, the original fluorescence decay data must be compensated. To do this, we measured a time course of the photobleaching of completely photoconverted Phamret. We then divided the originally acquired decay curve by the photobleaching curve and used the recalculated data for the curve fitting. Using the values of K and w, we fitted the FDAP decay curves of $I_{\text{rel. image}^*}(t)$ to the decay function, $I_{\text{rel. calc.}}(t)$ modified from that reported for FRAP[27]:

$$I_{\text{rel. image}^*}(t) = \alpha \times I_{\text{rel. calc}}(t)$$

$$= \alpha\left(1 - \left(1-\beta\right)\sum_{n=0}^{+\infty}\frac{(-K)^n}{n!}\left(1+n\left(1+\frac{2t}{\tau_D}\right)\right)^{-1} + \beta\frac{1-e^{-K}}{K}\right) \quad (3)$$

where α is a parameter to conform $I_{\text{rel. calc.}}$ to $I_{\text{rel. image}^*}$ at $t = 0$ and β is the fraction of immobile molecules (ranging from 0 to 1).

τ_D is the characteristic diffusion time related to the diffusion coefficient, D, by $\tau_D = w^2/4D$. The series solution for the fluorescence decay was truncated after 40 terms[18], assuring that the neglected terms made an insignificant contribution. All of the curve fittings were done by using a weighted least-squares algorithm implemented in Origin (OriginLab).

Additional methods. The methods for plasmid construction, cell culture and transfections, protein purification, gel filtration, spectroscopy, pH titration, measurement of photoconversion quantum yield and western blotting are available in **Supplementary Methods** online.

Note: Supplementary information is available on the Nature Methods website.

ACKNOWLEDGMENTS

We thank H. Kimura and Y. Yoneda (Osaka University) for providing the cDNA encoding H2B-GFP and PP2Cγ, and fibrillalin, respectively. We also thank D. Goto and I. Kotera for helpful comments. We also thank F. Inagaki and N. Noda for help with gel filtration analysis. This work was partially supported by grants from Scientific Research on Advanced Medical Technology of the Ministry of Labor, Health and Welfare of Japan, Precursory Research for Embryonic Science and Technology of the Japan Science and Technology Agency, and the Japanese Ministry of Education, Science and Technology.

AUTHOR CONTRIBUTIONS

T.M. performed experiments, analyzed data and prepared the manuscript; A.M. contributed to data analysis; T.N. contributed to the conceptual development and experimental design and performed experiments, analyzed data and prepared the manuscript.

Published online at http://www.nature.com/naturemethods/
Reprints and permissions information is available online at http://npg.nature.com/reprintsandpermissions

1. Lippincott-Schwartz, J., Snapp, E. & Kenworthy, A. Studying protein dynamics in living cells. *Nat. Rev. Mol. Cell Biol.* **2**, 444–456 (2001).
2. Zhang, J., Campbell, R.E., Ting, A.Y. & Tsien, R.Y. Creating new fluorescent probes for cell biology. *Nat. Rev. Mol. Cell Biol.* **3**, 906–918 (2002).
3. Miyawaki, A. Visualization of the spatial and temporal dynamics of intracellular signaling. *Dev. Cell* **4**, 295–305 (2003).
4. Medina, M.A. & Schwille, P. Fluorescence correlation spectroscopy for the detection and study of single molecules in biology. *Bioessays* **24**, 758–764 (2002).
5. Reits, E.A. & Neefjes, J.J. From fixed to FRAP: measuring protein mobility and activity in living cells. *Nat. Cell Biol.* **3**, E145–E147 (2001).
6. White, J. & Stelzer, E. Photobleaching GFP reveals protein dynamics inside live cells. *Trends Cell Biol.* **9**, 61–65 (1999).
7. Lukyanov, K.A., Chudakov, D.M., Lukyanov, S. & Verkhusha, V.V. Innovation: Photoactivatable fluorescent proteins. *Nat. Rev. Mol. Cell Biol.* **6**, 885–891 (2005).
8. Patterson, G.H. & Lippincott-Schwartz, J. A photoactivatable GFP for selective photolabeling of proteins and cells. *Science* **297**, 1873–1877 (2002).
9. Verkhusha, V.V. & Sorkin, A. Conversion of the monomeric red fluorescent protein into a photoactivatable probe. *Chem. Biol.* **12**, 279–285 (2005).
10. Chudakov, D.M. *et al.* Kindling fluorescent proteins for precise *in vivo* photolabeling. *Nat. Biotechnol.* **21**, 191–194 (2003).
11. Ando, R., Mizuno, H. & Miyawaki, A. Regulated fast nucleocytoplasmic shuttling observed by reversible protein highlighting. *Science* **306**, 1370–1373 (2004).
12. Ando, R., Hama, H., Yamamoto-Hino, M., Mizuno, H. & Miyawaki, A. An optical marker based on the UV-induced green-to-red photoconversion of a fluorescent protein. *Proc. Natl. Acad. Sci. USA* **99**, 12651–12656 (2002).
13. Wiedenmann, J. *et al.* EosFP, a fluorescent marker protein with UV-inducible green-to-red fluorescence conversion. *Proc. Natl. Acad. Sci. USA* **101**, 15905–15910 (2004).
14. Chudakov, D.M. *et al.* Photoswitchable cyan fluorescent protein for protein tracking. *Nat. Biotechnol.* **22**, 1435–1439 (2004).
15. Tsutsui, H., Karasawa, S., Shimizu, H., Nukina, N. & Miyawaki, A. Semi-rational engineering of a coral fluorescent protein into an efficient highlighter. *EMBO Rep.* **6**, 233–238 (2005).
16. Gurskaya, N.G. *et al.* Engineering of a monomeric green-to-red photoactivatable fluorescent protein induced by blue light. *Nat. Biotechnol.* **24**, 461–465 (2006).
17. Ballestrem, C., Wehrle-Haller, B. & Imhof, B.A. Actin dynamics in living mammalian cells. *J. Cell Sci.* **111**, 1649–1658 (1998).
18. Phair, R.D. & Misteli, T. High mobility of proteins in the mammalian cell nucleus. *Nature* **404**, 604–609 (2000).
19. Llopis, J., McCaffery, J.M., Miyawaki, A., Farquhar, M.G. & Tsien, R.Y. Measurement of cytosolic, mitochondrial, and Golgi pH in single living cells with green fluorescent proteins. *Proc. Natl. Acad. Sci. USA* **95**, 6803–6808 (1998).
20. Recalcati, S., Menotti, E. & Kühn, L.C. Peroxisomal targeting of mammalian hydroxyacid oxidase 1 requires the C-terminal tripeptide SKI. *J. Cell Sci.* **114**, 1625–1629 (2001).
21. Kimura, H. & Cook, P.R. Kinetics of core histones in living human cells: little exchange of H3 and H4 and some rapid exchange of H2B. *J. Cell Biol.* **153**, 1341–1353 (2001).
22. Gerlich, D. *et al.* Global chromosome positions are transmitted through mitosis in mammalian cells. *Cell* **112**, 751–764 (2003).
23. Pack, C., Saito, K., Tamura, M. & Kinjo, M. Microenvironment and effect of energy depletion in the nucleus analyzed by mobility of multiple oligomeric EGFPs. *Biophys. J.* **91**, 3921–3936 (2006).
24. Braga, J., Desterro, J.M.P. & Carmo-Fonseca, M. Intracellular macromolecular mobility measured by fluorescence recovery after photobleaching with confocal laser scanning microscopes. *Mol. Biol. Cell* **15**, 4749–4760 (2004).
25. Meyvis, T.K., De Smedt, S.C., Van Oostveldt, P. & Demeester, J. Fluorescence recovery after photobleaching: a versatile tool for mobility and interaction measurements in pharmaceutical research. *Pharm. Res.* **16**, 1153–1162 (1999).
26. Axelrod, D., Koppel, D.E., Schlessinger, J., Elson, E. & Webb, W.W. Mobility measurement by analysis of fluorescence photobleaching recovery kinetics. *Biophys. J.* **16**, 1055–1069 (1976).
27. Calapez, A. *et al.* The intranuclear mobility of messenger RNA binding proteins is ATP dependent and temperature sensitive. *J. Cell Biol.* **59**, 795–805 (2002).
28. Shimozono, S. *et al.* Concatenation of cyan and yellow fluorescent proteins for efficient resonance energy transfer. *Biochemistry* **45**, 6267–6271 (2006).

Cell-cycle-specific nestin expression coordinates with morphological changes in embryonic cortical neural progenitors

Takehiko Sunabori[1,2,3], Akinori Tokunaga[1,3], Takeharu Nagai[4,5], Kazunobu Sawamoto[1,2], Masaru Okabe[6], Atsushi Miyawaki[4], Yumi Matsuzaki[1], Takaki Miyata[7] and Hideyuki Okano[1,3,*]

[1]Department of Physiology, [2]Bridgestone Laboratory of Developmental and Regenerative Neurobiology, Keio University School of Medicine, Tokyo 160-8582, Japan
[3]Solution Oriented Research for Evolutional Science and Technology (SORST), Japan Science and Technology Agency (JST), Saitama 332-0012, Japan
[4]Laboratory for Cell Function and Dynamics, Advanced Technology Development Center, Brain Science Institute, RIKEN, Saitama 351-0198, Japan
[5]Laboratory for Nanosystems Physiology, Research Institute for Electronic Science, Hokkaido University, Hokkaido 060-0812, Japan
[6]Genome Information Research Center, Research Institute for Microbial Diseases, Osaka University, Osaka 565-0871, Japan
[7]Department of Anatomy and Cell Biology, Graduate School of Medicine, Nagoya University, Nagoya 466-8550, Japan
*Author for correspondence (e-mail: hidokano@sc.itc.keio.ac.jp)

Accepted 24 January 2008
Journal of Cell Science 121, 1204-1212 Published by The Company of Biologists 2008
doi:10.1242/jcs.025064

Summary

During brain development, neural progenitor cells extend across the thickening brain wall and undergo mitosis. To understand how these two completely different cellular events are coordinated, we focused on the transcription pattern of the nestin gene (*Nes*), which encodes an intermediate filament protein strongly expressed in neural progenitor cells. To visualize nestin expression in vivo, we generated transgenic mice that expressed a destabilized fluorescent protein under the control of *Nes* second intronic enhancer (E/nestin:dVenus). During the neurogenic stage, when the brain wall thickens markedly, we found that nestin was regulated in a cell-cycle-dependent manner. Time-lapse imaging showed that nestin gene expression was upregulated during G1-S phase, when the neural progenitor cells elongate their fibers. However, nestin expression dramatically declined in G2-M phase, when progenitor cells round up to undergo mitosis. The cell-cycle-dependent phosphorylation of an upstream regulator class III POU transcription factor (Pou3f2 or Brn2) reduced its binding activity to the nestin core enhancer element and was therefore responsible for the decreased *Nes* transcription in G2-M phase. Collectively, these findings demonstrate precisely orchestrated gene regulation that correlates with the 3D morphological changes in neural progenitor cells in vivo.

Supplementary material available online at
http://jcs.biologists.org/cgi/content/full/121/8/1204/DC1

Key words: Intermediate filament, Phosphorylation, Radial glia, POU, SOX, Cell cycle

Introduction

During brain development, the primordium of each brain region, initially composed purely of neural progenitor cells (Okano, 2002), thickens as newly generated neurons accumulate between the ventricle and the pia. There are marked stage-dependent changes in the morphology of the progenitor cells in the developing cerebral cortex during the time that brain-wall thickening is most prominent (Takahashi et al., 1993) (summarized in Fig. 5A). Initially, in embryonic day (E) 9 to E11 mice, progenitor cells, called neuroepithelial cells, span the cerebral wall, crossing distances of up to 100 μm. As development proceeds, the progenitor cells adopt a radially elongated morphology connected to the ventricular and pial surfaces (also called 'radial glial' cells) (Rakic, 2003). Their extended processes span 200-300 μm by E13-E14 and 400-500 μm at E15-E16.

Although newborn progenitor cells must adapt to the developmental stage-specific changes in brain wall thickness, they must also alter their morphology in a cell-cycle-dependent manner (summarized in Fig. 5B). At the beginning of G1 phase, each progenitor cell generated at the ventricular surface either lacks its pial process (Hinds and Ruffett, 1971) or is connected to the pial surface, depending on whether or not it inherited the pial process from the parent cell (Miyata et al., 2001; Noctor et al., 2001). The daughter lacking the pial process (Fig. 5B, arrowhead ii) elaborates a new one, mainly during G1 phase, and subsequently adopts a bipolar 'radial glial' morphology by the time it reaches S phase (Miyata et al., 2001; Noctor et al., 2002). The daughter that inherited the pial process (Fig. 5B, arrowhead i) must also elongate its process to span the thickening cerebral wall, and must do so within a single cell cycle (Takahashi et al., 1993). Although the elongated processes of neural progenitor cells have long been known to serve as a scaffold for migrating newborn neurons (Rakic, 1972), how their polarized and elongated morphology is established during brain development remains unclear. Here we ask, what is the 'trick' that enables a progenitor cell to undertake two completely different jobs (elaborating a process and dividing) that must be carefully coordinated?

To approach this question, we focused on the transcriptional pattern of the nestin gene (*Nes*) for two reasons. First, nestin is strongly expressed in neural progenitor cells (Hockfield and McKay, 1985). Second, *Nes* encodes an intermediate filament (IF) protein (Lendahl et al., 1990), which comprises one of the three major

cytoskeletal systems. Furthermore, a recent report showed that IFs are involved in the establishment of the bipolar morphology and also the twisting of the pial process that influences the kinetics of neural progenitor nuclear movement (Miyata and Ogawa, 2007). Moreover, several papers have shown that nestin is important in regulating the assembly or disassembly of the IF network (Sahlgren et al., 2001; Chou et al., 2003), and it has been proposed to function as a crossbridge with other cytoskeletal systems (Marvin et al., 1998). Thus, we predicted that the transcription of *Nes* might be coordinated with the stage- or cell-cycle-dependent morphological alteration of neural progenitor cells. To elucidate the mechanism for regulating *Nes* expression, we observed its transcription pattern in vivo, relative to cell development and the cell cycle.

Results

Expression pattern of E/nestin:dVenus transgene in the developing CNS

To evaluate accurate *Nes* expression, we needed a new tool, because the previously established transgenic mice expressed EGFP under control of the *Nes* second intronic enhancer (Kawaguchi et al., 2001). EGFP is stable for too long to be used in evaluating changes that occur within such a short period as a single cell cycle. Therefore, we generated transgenic mice expressing destabilized Venus (dVenus) under the control of the same driver – the *Nes* second intronic enhancer (E/nestin:dVenus; Fig. 1A). Venus is a GFP derivative made from YFP and contains mutations that greatly accelerate the maturation of the fluorescent protein at 37°C. It also shows 10- to 100-fold stronger fluorescence than YFP in vitro (Nagai et al., 2002). In the dVenus construct, a PEST amino acid sequence from mouse ornithine decarboxylase is fused to the C-terminus of Venus, thus targeting the protein for rapid, cell-cycle-independent intracellular degradation (Li et al., 1998; Corish and Tyler-Smith, 1999). Therefore, the dVenus reporter cassette allows the strict on-off enhancer-promoter activity to be detected as a fluorescent signal (Kohyama et al., 2005).

Four independent mouse lines showed virtually identical dVenus expression patterns, indicating that its expression profile was consistent regardless of the transgene insertion site. dVenus was first detected around E8.5 throughout the central nervous system (CNS) and the signal became much weaker by E17.5 (data not shown).

We first observed coronal sections of the developing forebrain of E/nestin:dVenus transgenic mice. The dVenus fluorescence was localized strictly to the ventricular zone (VZ) at all developmental stages (supplementary material Fig. S1). Because our focus was on the regulation of *Nes* transcription, we also studied the expression patterns of molecules from candidate regulator genes. The *cis*-element of *Nes* used to drive dVenus expression has been extensively studied, and the evolutionarily conserved region in the 3′ half of the second intron contains an enhancer that is synergistically regulated by group B1 SOXs (SOX1-SOX3) and class III POU (Pit-Oct-Unc) transcription factors (Zimmerman et al., 1994; Lothian and Lendahl, 1997; Josephson et al., 1998; Tanaka et al., 2004). We found that the expression of both transcription factors roughly paralleled that of the dVenus expression during neurogenesis (supplementary material Fig. S1).

Usefulness of E/nestin:dVenus mice and correlation between fluorescence intensity and *Nes* mRNA expression

To confirm that the dVenus expression pattern of our novel transgenic mice faithfully reproduced the expression pattern of endogenous nestin, we first compared the dVenus expression from our transgenic mice with the EGFP pattern of E/nestin:EGFP mice, in which the EGFP sequence is driven by the same regulatory sequence as in the dVenus-expressing transgenic mice (Kawaguchi et al., 2001). To evaluate the transgenic lines under the same conditions, we mated E/nestin:dVenus with E/nestin:EGFP transgenic mice and generated a double-transgenic embryo. Because dVenus is a modified YFP, their emission spectra were close (Fig. 1B). To separate the signals from the same section, we used the linear unmixing function of the confocal laser-scanning microscope LSM510 META (Zeiss). Brains from E14.5 embryos expressing both transgenes were sectioned and counterstained with an antibody to β-tubulin III, an early neuronal marker (Fig. 1C,D). We found that the dVenus-expressing cells were entirely included within the population of EGFP-positive cells in the VZ, and there was no overlap between dVenus expression and β-tubulin-III-expressing neurons (Fig. 1D). However, some EGFP-positive cells were double-labeled for β-tubulin III, and the EGFP signal persisted in cells in the intermediate zone, even after their neuronal differentiation (Fig. 1D, arrowheads). These results indicated that the E/nestin:dVenus transgenic mice expressed dVenus only in cells that had not differentiated into neurons, showing that the dVenus fluorescence was more faithful to the nestin expression pattern than the EGFP fluorescence driven by the same enhancer.

To determine the correlation between dVenus expression and the differentiation state, we sorted cerebral wall cells from dVenus transgenic embryos by fluorescence-activated cell sorting (FACS). Cells were fractionated into dVenus-positive (F2) and -negative (F1) populations, following the profile of the negative control from wild-type mouse brain (Fig. 1E). We characterized the cells in each fraction using antibodies against nestin and β-tubulin III. As expected, nestin-expressing cells were abundant (96.4±1.2%) in the F2 fraction, and made up less (26.9±1.0%) of the F1 fraction. The relative abundance of the β-tubulin-III-positive cells was reciprocal to that of the nestin-expressing cells: they made up 0.7±1.0% of the cells in F2 and 80.3±6.4% of the cells in F1 (Fig. 1F).

To confirm the accuracy of the sorting process, we also used an anti-GFP antibody to label dVenus. We found that the dVenus-expressing cells were reliably sorted into the F2 fraction (94.7±2.5%) and were almost absent from the F1 fraction (1.0±0.3%) (Fig. 1F). Moreover, cells from the F2 fraction formed self-renewable and multipotent neurospheres at a much higher rate (16±1 cells/500 cells) than those from the F1 fraction (0.2±0.4 cells/500 cells) (supplementary material Fig. S2B,C). These observations confirmed that our new dVenus reporter transgenic mice were more useful than the E/nestin:EGFP transgenic mice for characterizing neural stem/progenitor cells.

To determine the correlation between *Nes* mRNA expression and dVenus fluorescence intensity, we subdivided the dVenus-positive fraction (F2) into equal subfractions containing the high (F4) and low (F3) transgene-expressing-cells, based on fluorescence intensity (Fig. 1E). The level of *Nes* mRNA in the dVenus (and largely nestin)-positive progenitor populations (F3 and F4) and the dVenus-negative fraction (F1) was determined by real-time quantitative PCR. The fluorescence intensity of the E/nestin:dVenus cells exhibited a positive correlation with the amount of *Nes* mRNA (Fig. 1G), indicating that the reporter expression reflects the actual expression of *Nes* mRNA. Therefore, we monitored the expression level of *Nes* mRNA via the fluorescence intensity of dVenus in vivo.

Cell cycle-dependent expression of *Nes* mRNA

Because EGFP is a stable protein, the level of fluorescence produced by E/nestin:EGFP was uniform throughout the embryonic VZ. By contrast, owing to the short half-life of dVenus, the fluorescence in the VZ of E/nestin:dVenus embryos showed scattered fluorescent cells (Fig. 1D). This observation was consistent with our idea that the enhancer activity of *Nes* might be regulated by the cell cycle in neural progenitors, particularly because the VZ contains proliferating cells in various cell cycle phases. Therefore, we focused on the relationship between dVenus expression and the cell cycle.

Each cell cycle phase was discriminated by labeling the cells for differing periods of time before sacrifice with thymidine analogues (Fig. 2A; see Materials and Methods for details). The cells that expressed dVenus were counted at each cell cycle phase. To label cells in S phase, IdU was injected into pregnant dams 30 minutes before sacrifice (Fig. 2B purple). A high proportion of cells in S phase expressed dVenus (Fig. 2B arrowheads; 63.3±5.2%). However, cells in G2-M phase, which were labeled by injecting IdU 3 hours before sacrifice (Fig. 2C red), showed hardly any dVenus expression (Fig. 2C arrows; 9.3±1.4%). dVenus expression was stronger (Fig. 2D arrowheads; 47.4±7.9%) in G1 phase cells, which were labeled by injecting IdU 14.5 hours before sacrifice (Fig. 2D red). To distinguish cells in S phase, BrdU was injected 30 minutes before sacrifice in all trials (Fig. 2B-D purple). These data strongly support the hypothesis that *Nes* expression is regulated in a cell-cycle-dependent manner within the VZ, with expression being downregulated during G2-M phase (Fig. 2E).

Nes is strongly expressed in radially elongating G1-phase VZ cells and is downregulated in G2-M phase

Cortical progenitor cells positive for nestin protein show dynamic morphological changes in vivo (summarized in Fig. 5). Because pharmacological depolymerization of IFs by calyculin-A affects the bipolar morphology of neural progenitor cells in vivo (Miyata and Ogawa, 2007), we next explored the relationship between *Nes* expression and the three-dimensional (3D) morphology of the neural progenitor cells, especially the radial glial cells. To visualize live radial glial cells, we placed DiI on the pial surface of the cerebrum and performed time-lapse imaging of cerebral wall slices. Radial glialcells are known to retain the radial process during mitosis, and the fiber is inherited by one of the daughter cells (Miyata et al., 2001; Noctor et al., 2001). Fig. 3A shows a series of time-lapse imaging of a pair of daughter cells 4 hours after their birth at the ventricular surface. The daughter cell that did not inherit the radial fiber (Fig. 3A, arrowhead ii) began to extend a new pial process, and its sister cell (Fig. 3A, arrowhead i) thickened and extended its inherited fiber 20 μm according to the brain wall thickening within this period (Fig. 3A, *). The strong expression of dVenus observed in both of the newly born daughter cells (Fig. 3A) confirmed that the expression level increased during G1 phase, as we had observed in the BrdU/IdU labeling assay (Fig. 2). This observation also demonstrated that the dynamic activation of the *Nes* enhancer correlates with the 3D growth of cortical progenitor cells.

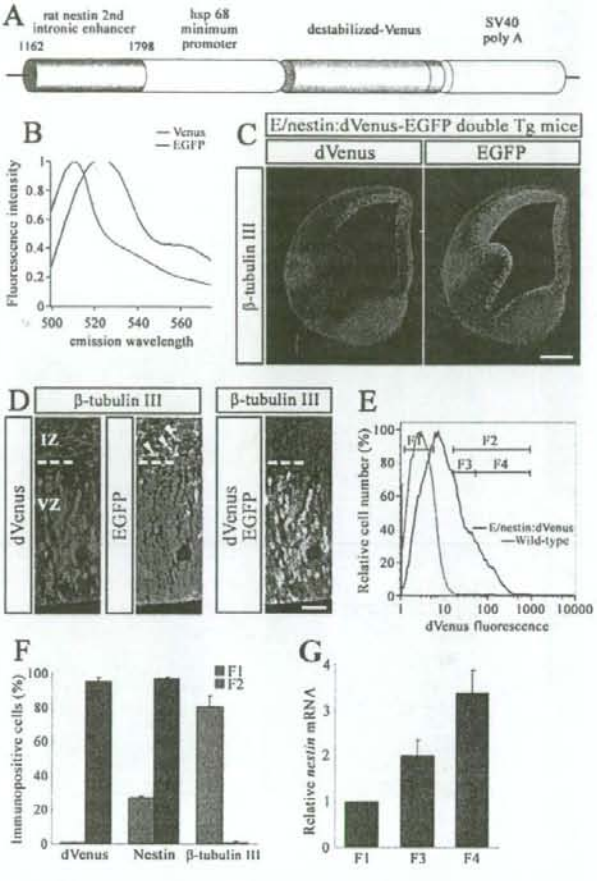

Fig. 1. E/nestin:dVenus fluorescence intensity is correlated with *Nes* mRNA expression. (A) Structure of the E/nestin:dVenus transgene. (B) Emission spectra of Venus (green) and EGFP (red). (C,D) On an identical section from an E14 E/nestin:dVenus-EGFP double transgenic embryo, no dVenus-expressing cells showed immunoreactivity against the anti-β-tubulin III antibody, although some EGFP-expressing cells did (arrowheads). VZ, ventricular zone; IZ, intermediate zone. (E) Representative FACS profile of cerebral-wall-derived cells from an E14.5 E/nestin:dVenus transgenic embryo. (F) Quantitative data showing the percentage of E/nestin:dVenus negative (F1) and positive (F2) cells immunostained with nestin, β-tubulin III and GFP antibodies. (G) To compare the E/nestin:dVenus fluorescence intensity with the *Nes* mRNA expression level, real-time quantitative PCR was performed. dVenus-positive cells were subdivided into two fractions based on their fluorescence intensity: high (F4) and low (F3). The *Nes* mRNA expression level of these two fractions (F4 and F3), as well as of the dVenus-negative cells (F1), showed a positive correlation with the fluorescence intensity. Data are means ± s.e.m. Scale bars: 500 μm (C), 25 μm (D).

Because the nuclear movement towards the ventricular surface (adventricular migration) is characteristic of G2 phase progenitor cells (Hayes and Nowakowski, 2000), we next asked whether progenitor cells whose nucleus was translocating toward the ventricular surface would show downregulated dVenus expression, as the BrdU/IdU labeling suggested (Fig. 2). As expected, dVenus was consistently undetectable in these G2-phase cells (Fig. 3B)